HHS Public Access

Author manuscript

NMR Biomed. Author manuscript; available in PMC 2017 April 01.

Published in final edited form as:

NMR Biomed. 2017 April ; 30(4): . doi:10.1002/nbm.3546.

CONTRIBUTIONS TO MAGNETIC SUSCEPTIBILITY OF BRAIN TISSUE

Jeff H. Duyn[+,*] and **John Schenck**[++]

[+]Advanced MRI Section, Laboratory of Functional and Molecular Imaging, National Institutes of Neurological Disorders and Stroke, National Institutes of Health, Bethesda, Maryland 20892, USA

[++]MRI Technologies and Systems, General Electric Global Research Center, 1 Research Circle, Schenectady, New York 12309, USA

Abstract

This review discusses the major contributors to the subtle magnetic properties of brain tissue and how they affect MRI contrast. With the increased availability of high field scanners, the use of magnetic susceptibility contrast for the study of human brain anatomy and function has increased dramatically. This not only has led to novel applications, but also has improved understanding of the complex relationship between MRI contrast and magnetic susceptibility. Chief contributors to magnetic susceptibility of brain tissue have been found to include myelin as well as iron. In the brain, iron exists in various forms with diverse biological roles, many of which are only now starting to be uncovered. An interesting aspect of magnetic susceptibility contrast is its sensitivity to the microscopic distribution of iron and myelin, which provides opportunities to extract information at spatial scales well below the MRI resolution. For example, in white matter, the myelin sheath that surrounds axons can provide tissue contrast that is dependent on axonal orientation and reflect the relative size of intra- and extra-axonal water compartments. Extraction of such ultra-structural information, together with quantitative information about iron and myelin concentrations is an active area of research geared towards characterization of brain structure and function and their alterations in disease.

Keywords

magnetic susceptibility; iron; myelin

INTRODUCTION

MRI is exquisitely sensitive to the subtle variations in magnetic susceptibility across the human brain, especially when using so-called “susceptibility-weighted” (SW) techniques like gradient-echo MRI at high field. These techniques are increasingly being used to study the brain’s vasculature, and regional variations in tissue myelin and iron content. At high field, they provide exquisite anatomical detail not available with other techniques (Figure 1) (1,2). SW contrast also forms the basis of blood oxygenation level dependent (BOLD) fMRI,

[*]Corresponding author: Tel: 301-594-7305, jhd@helix.nih.gov.

which has revolutionized the study of brain activity by recording the susceptibility changes resulting from changes in blood oxygenation (3).

Along with the optimization and increased use of SW MRI, major advances have been made in the understanding of its contrast mechanisms. For example, it is now well understood that susceptibility contrast is not only affected by tissue composition, but also by the orientational order resulting from its cellular and molecular structure. At the same time, further details about the complex biological role of iron, a primary contribution to magnetic susceptibility, are becoming available. Here, we will review recent progress in the understanding and interpretation of magnetic susceptibility contrast and how this is applied to study changes with disease. The review is written in the context of previous literature that has reviewed this topic in the past (4–7).

TISSUE MAGNETIC SUSCEPTIBILITY

Magnetic susceptibility refers to the magnetizability of a material when placed in a magnetic field B_0. It is indicated with the symbol χ, which represents a proportionality constant between the material's macroscopic magnetization M and local magnetic field B ($M = \chi \frac{B}{\mu_0} \approx \chi \frac{B_0}{\mu_0}$, with μ_0 a physical constant representing the magnetic permeability of vacuum, and equal to $4\pi \cdot 10^{-7}$ H m^{-1}). A material's χ is dependent on its molecular constituents, and originates from spins and motions of nuclei and their electrons. χ can be positive or negative, reflecting whether magnetization aligns with the field (paramagnetism), or opposes it (diamagnetism). Paramagnetism generally originates from field-induced alignment of unpaired electron spins, whereas diamagnetism is associated with field-induced alteration of electron orbits (8).

Each electron of an atom has a spin of $s = \pm ½$ and the total spin, S, is the sum of the spins of each individual valence electron. The vast majority of biological molecules have even numbers of electrons and all their spin-up electrons are paired with spin-down electrons giving each of these molecules a total spin $S = 0$. These are called closed shell molecules and have a very feeble negative magnetizability and are called diamagnetic. For many purposes (but not in MRI) this effect can be ignored and the molecules are then called nonmagnetic.

A very small fraction of biological molecules, especially those containing transition metal elements such as iron, copper and manganese, have unpaired valence electrons. This gives these open shell molecules and ions a magnetizability of the opposite sign and roughly a thousand times stronger than that of closed shell structures. Using heme in hemoglobin as an example the magnetic behavior of ferric and ferrous iron ions is indicated in Figure 2. The *d*-shell of iron provides five energy levels or orbitals each potentially containing one spin-up and one spin-down electron. Spherical harmonics corresponding to these orbitals are indicated on the left of the figure. Here the *z*-axis is perpendicular to the plane of the heme and $r^2 = x^2 + y^2$. The spin degree of freedom leads to the *d*-shell providing a total of ten spin orbitals that may be occupied by valence electrons. Ferrous iron has six valence electrons to distribute over these ten spin orbitals and ferric iron has five. A paramagnetic molecule or

ion will have a total magnetic moment, m, given by $m = \mu_{eff}\mu_B$ where $\mu_B = 9.274\ 10^{-24}$ J T^{-1} is the Bohr magneton. The effective number of Bohr magnetons, μ_{eff}, is often given quite accurately by the spin-only approximation, $\mu_{eff}=2\sqrt{S(S+1)}$ (8). Ions such as iron in the brain do not exist in isolation but interact with their environment. That is, they will be bonded to some degree to adjacent ions or molecules and these ligands will modulate the energy levels and the μ_{eff} of the spin orbitals. Therefore, the energy levels and spin values shown in Figure 2 are approximations and will be modified somewhat in a real situation depending on the details of the ligands bonded to the iron atom.

Human brain tissues have a rather weak (diamagnetic) magnetic susceptibility that is dominated by that of water (χ = −9.05 ppm) due to its large abundance (70–85% of brain tissue is water). Across grey and white matter of healthy brain, it varies within a range from about −9.2 to −8.8 ppm. This variation is primarily caused by variations in iron and myelin content, which both have sufficient concentration and susceptibilities sufficiently different from water to contribute substantially. Lipids in myelin are diamagnetic (relative to water), and as a result, heavily myelinated white matter is generally the most diamagnetic tissue in healthy brain. Somewhat outside the range for χ mentioned above is blood inside the venous vasculature, where iron in deoxyhemoglobin renders χ slightly more paramagnetic (fully deoxygenated blood: χ = −7.9 ppm). A wider range for χ may also be found under pathological conditions. For example, calcifications may result in a more diamagnetic χ(9), whereas accumulation of iron (e.g. associated with neurodegeneration or as a result of microbleeds) may render χ more paramagnetic. After a brief review of the effect of magnetic susceptibility on MRI, further details about the biological role, magnetic properties, and brain distribution of iron and myelin χ will be discussed below.

EFFECTS OF SUSCEPTIBILITY ON MRI

The effects of tissue susceptibility variations on the magnetic field can be studied with SW MRI through acquisition of one or multiple gradient echo signals, from which amplitude and frequency are extracted. Tissue susceptibility can affect both amplitude and frequency through the resonance frequency f of water ^{1}H protons, which depends on the field B they "sense" according to $f=\frac{\gamma}{2\pi}B$. B is a combination of the applied field (static field B_0 of the MRI scanner) and the field shift ΔB created by the magnetization M of the object. With the latter relating to χ according to $M \approx \chi\frac{B_0}{\mu_0}$, we have $\Delta B = \mu_0 M = \chi B_0$. Although variations in χ are generally small (on the order of 0.1 ppm), they can lead to easily detectable frequency shifts that scale with static field strength: at 7 T, typical frequency shifts are on the order of a few Hz.

The field shift ΔB resulting from a spatially varying $M(r)$ can be found by (spatially) convolving M with the magnetic field generated by a point dipole (an infinitely small magnet with unit magnetization). For the simple case of an infinitely extending uniform magnetization M this dipole convolution leads to a uniform field shift $\Delta B = \mu_0 M$; an outer boundary that is geometrically simple (e.g. cylinder, sphere), leads to an additional field shift that can be taken into account by the use of so-called "demagnetization", "demagnetizing",

or "shape" factors (here indicated with *S*), which e.g. for a sphere results in a subtraction of a factor $\frac{1}{3}\mu_0 M$ (10).

Unfortunately, further complication results from the fact that, while χ and M are defined macroscopically, mechanistically they result from (sub-) atomic scale dipoles. Thus, only with gross simplification (and ignoring statistical mechanics) is it possible to characterize the actual field ΔB sensed by a water ^{1}H proton. Commonly used is the so-called "Lorentz sphere" approach, which models the sensing nucleus to reside in a spherical cavity, surrounded by a macroscopic continuum magnetization (see e.g. (10,11)) (Figure 3). Again, considering uniform magnetization and using shape factors, the spherical inner boundary of the magnetization (outer boundary of cavity) leads to $\Delta B = \frac{1}{3}\mu_0 M$ (see e.g. (11)). Interestingly, in the aforementioned situation of a finite object with spherical outer boundary, we would have $\Delta B = \frac{1}{3}\mu_0 M - \frac{1}{3}\mu_0 M = 0$, leading to the somewhat counter-intuitive finding that the average, magnetization-related field shift sensed by water protons (ΔB)is zero inside a spherical, uniformly magnetized object!

To estimate the magnitude of frequency shifts in brain tissue, we consider the simple case of a long cylinder of uniform magnetization aligned with the direction of B_0 (e.g. a blood vessel or white matter fiber bundle), in which case we have $S = 0$ (identical to the case of an infinitely extending object), resulting in $\Delta B = \frac{1}{3}\mu_0 M$, and leading to $\Delta f = \frac{\gamma}{2\pi}\frac{1}{3}\chi B_0$, which at 7 T is about 100 Hz for each ppm in susceptibility. Since SW MRI can easily pick up shifts as small as 0.1 Hz (2), susceptibility shifts of only 1 ppb are in principle detectable! This offers unique opportunities to quantify and map subtle variations in tissue iron and myelin content.

Of course, this is not the entire story. Other than macroscopic object boundaries and atomic-scale structure, tissues generally possess structure at various intermediate scales, which complicates interpretation of field shifts in terms of voxel-averaged χ values and underlying variation in tissue constituents. To the extent that this structure is captured by the MRI resolution, its effect can be accounted for by the use of shape factors, or more generally by deconvolution methods, both based on information available from the MRI image. The latter allows one to directly translate frequency distributions into images of χ. This so-called "quantitative susceptibility mapping" (QSM) is a very active area of research and one of tremendous recent progress (for reviews, see (12,13)). Structure that exists on the sub-voxel scale and is not captured by MRI may also confound the interpretation of frequency shifts, as has been emphasized recently (14). Accounting for such structure requires assumptions about its geometry and orientation, and necessarily requires gross simplification. An established approach is to consider the average magnetic environment of water protons in a voxel (10,15,16). Due to the extensive spatial and motional averaging, this average environment may be approximated to have a relatively simple shape (e.g. cylindrical, ellipsoidal, or spherical), in which case their effect on ΔB may be estimated by (again) the use of shape factors (see also the section on tissue structure below).

There are also a couple of caveats with the measurement of frequency shifts: In MRI, field estimates are based on the voxel-averaged resonance frequency of water protons, and thus weighted by their NMR visibility. The latter can be affected by the local environment through relaxation times T_1, T_2, and T_2*, diffusional motion, and magnetization transfer. Secondly, MRI frequency measurements may be sensitive to factors other than susceptibility including e.g. temperature and image artifacts caused by motion, drift, respiration etc.

Field variations are not only reflected in the signal phase and frequency, but may affect amplitude as well. In the absence of motional averaging of the field sensed by protons, field variations within a voxel will result in a distribution of resonance frequencies, leading to a decoherence and signal loss of the proton signals that increases with echo time. By comparing signals acquired at different echo times, the signal decay rate can be quantified. Generally, single-exponential signal decay (rate indicated with R_2*) is assumed, and the decay rate is interpreted as (partly) reflecting the strength of the susceptibility variations.

Both χ and R_2* can be used to study the concentration of susceptibility perturbers such as iron, myelin and deoxyhemoglobin. It is also possible to directly (without calculating χ and R_2*) combine signal amplitude and phase into a single image (17): this may facilitate the visual identification of focal changes in susceptibility and has been applied clinically to visualize vascular abnormalities and local iron accumulation in a range of pathologies (18).

Signal amplitude, phase (and frequency) and extracted parameters R_2* and χ all have been used to improve visualization of detailed anatomical structures, predominantly at 7 T. This includes neo-cortical sub-structure (19–21), the hippocampal and perirhinal cortex (22–24), and many other GM regions including the subthalamic nucleus (25), the zona incerta (26,27), the basal ganglia (28,29), and the substantia nigra (30,31). Many of these sub-cortical GM regions are important targets and surgical landmarks for deep brain stimulation (32).

BRAIN DISTRIBUTION OF IRON

Iron in Brain Tissue

Much of MRI visible iron in tissue is located in ferritin and hemosiderin, associated with proteins that facilitate storage and transport (33). Excessive amounts outside such storage forms may be toxic, result in oxidative stress, and lead to disease (34). In healthy adult brain, total iron concentration varies from 0–≈200 μg per gram tissue, i.e. 200 ppm, with typical white matter (WM) and cortical grey matter (GM) regions being at the lower end of this range (< 60 ppm) (35,36). At the microscopic scale, strong variation exists across cell types, with microglia and oligodendrocytes staining most consistently for iron (36–40). Across WM, macroscopically, variable iron staining is observed, with subcortical WM often showing a “patchy” or “speckled” appearance (see e.g. Figs. 1 and 5)(37,39), and major fiber bundles such as the corpus callosum and optic radiations showing little staining (40). In GM, highest iron concentrations (up to ≈ppm) are found in the dentate nuclei of the cerebellum, and in central brain regions such as the basal ganglia and red nuclei, and often associated with glial cells (37,41). The lower concentrations found in cortex are often associated with oligodendrocytes (37,41).

Most pathological conditions are associated with increased tissue iron content, primarily in the form of hemosiderin and ferritin. Iron in hemosiderin near sites of prior vascular injury may originate from extravasated blood. More widespread increases occur with iron storage diseases such as aceruloplasminemia, where 2–3 fold increases in iron have been found across much of the brain (42). In many neurological diseases, iron accumulates preferentially in the basal ganglia (for reviews see (34,43,44)), regions where also other metals such as manganese (45) and gadolinium (46) have been found to accumulate. It is possible that the brain uses these regions as storage or dump for materials is does not need. In the rather common neurological disorder, restless leg syndrome, a decrease in iron tissue accumulation is present (47).

Iron in Blood

In blood, iron is predominantly associated with deoxyhemoglobin and normally present at concentrations of about 500 ppm, which is several-fold higher than in healthy tissue. Iron's paramagnetism changes with blood oxygenation state: fully deoxygenated, it renders blood susceptibility χ_{deoxy} about 1.2 ppm paramagnetic relative to water (48,49), whereas this paramagnetic behavior vanishes at 100% oxygenation. Thus MRI voxels within or near large vessels experience phase shifts and changes in R_2^* that depend on blood oxygenation level (50). This phenomenon provides the mechanism for BOLD contrast in fMRI (3). It also provides an opportunity to look at venous oxygenation and possibly oxygen extraction fraction by studying susceptibility shifts in large veins calculated from the phase shift created in their vicinity. This can be based on R_2^* (51,52) or χ (53)

The oxygenation of blood (and thus the oxygenation state of hemoglobin) varies considerably across the brain's vasculature: where arterial and capillary blood oxygenation may reach 80–90%, in the venous vasculature this may drop to 60% or lower, which corresponds to $\Delta\chi_{vein} \approx 0.5$ ppm. This makes SW MRI preferentially sensitive to the venous vasculature and explains its success in venographic applications (54).

In addition to the oxygenation level, the contribution of blood to the MRI signal depends on its local concentration (i.e. blood volume). Averaged over a size scale of a typical MRI voxel, cerebral blood volume (CBV) may range from 2–4%. Assuming 60% oxygenation, this contributes about 10–20 ppb to the overall susceptibility of tissue. As will be seen in the following sections, this is generally small relative to the contribution of other substances and therefore may contribute little to contrast observed between tissue types observed in SW MRI studies of anatomy (55).

Nevertheless, CBV can be locally significantly higher and is known to substantially vary over brain regions (56,57). Extreme examples are large veins such as the sagittal sinus, or the choroid plexus. As the size of these structures is similar or larger than the typical MRI resolution, apparent CBV values may approach 100%. Thus, the sensitivity of BOLD fMRI and vascular contrast in venography based on SW MRI will vary over brain regions and may accentuate larger veins. This is especially the case for vessels angled with B_0, where field changes extend to surrounding tissue and increase the contrast.

Pathological conditions can not only result in changes in vascular anatomy and oxygenation that may be picked up with SW MRI (58), but may also lead to extravasation of blood. For example, hemorrhagic stroke and traumatic brain injury may cause bleeding into tissue surrounding vessels, and the associated paramagnetic effects can be detected with SW MRI (59). With time, extravasated blood will break down and its iron will be sequestered in hemosiderin, which also has paramagnetic properties and often remains detectable with SW MRI.

EFFECT OF IRON ON MRI CONTRAST

The contribution of iron to the magnetic susceptibility of brain tissue is not only dependent on concentration, but potentially also on form and associated type of magnetism. For ferritin, theoretical estimates indicate that the contribution of iron to χ ($\Delta\chi_{iron}$) is 1.4 ppb for each ppm weight fraction of iron (i.e. for each μg iron per gram tissue, see Table 1) (49). This is based on a theoretical estimate of 520 ppm for χ of a ferritin particle fully loaded with 4500 Fe^{+++} ions. Magnetometry and MRI measurements with QSM on ferritin phantoms, in-vivo, and ex-vivo brain indicate a range for $\Delta\chi_{iron}$ of 0.55–1.3 ppb per ppm iron, somewhat below the theoretical estimate (60–67). Although the reason for this is unknown, it appears that χ of a ferritin particle may be somewhat below 520 ppm as would be expected if the ferritin iron loading is incomplete.

Due to field inhomogeneities across an MRI voxel associated with iron (e.g. ferritin particles), also the apparent signal decay rate R_2^* (as well as R_2', which excludes effects on the decay other than those caused by field inhomogeneities) may provide a measure of iron concentration (68). Theoretical estimates that assume spherical particles, and ignore effects of water diffusion, suggest R_2' increases by about 0.11 s^{-1} per Tesla static field for each ppb in $\Delta\chi_{iron}$ (69). Assuming $\Delta\chi_{iron}$ to be 1 ppb for each ppm weight fraction of iron (see above), we would expect R_2' to change by 0.11 s^{-1} T^{-1} per ppm iron. This is about two-fold higher than inferred from measurements, which indicate a range of 0.037 to 0.055 s^{-1} T^{-1} per ppm iron for R_2^* (which should increase by at least as much as R_2') (66,70,71). Similarly, studies of the relationship between R_2^* and $\Delta\chi_{iron}$ found a proportionality constant of around 0.05 (range 0.047–0.052) s^{-1} T^{-1} per ppb in $\Delta\chi_{iron}$ (72,73), again about half of the theoretical estimate of 0.11 s^{-1} T^{-1} per ppb in $\Delta\chi_{iron}$.

A possible explanation for the lower than expected effect of iron on R_2^* is the phenomenon of diffusion averaging. When spins diffuse through field gradients around a ferritin particle, differences (i.e. decoherence) between their accumulated phases may be reduced, reducing R_2^*. To evaluate the likelihood of this effect contributing, one can consider practical values for diffusion constant D, the particle radius R, and its susceptibility $\Delta\chi$ (69,74). Substantial phase accumulation near a particle occurs at time $\tau = \frac{1}{\Delta\omega}$, which at 7 T equals 3 μs ($\Delta\chi$ = 520 ppm). With $D \approx 1\ \mu m^2\ ms^{-1}$, the diffusion distance in time τ is $\sqrt{\tau D} = 55\ \mathrm{nm}$, which is substantially larger than the radius of an isolated ferritin particle, i.e. ~ 6 nm (summarized: diffusion substantially affects R_2^* when $\frac{D}{\Delta\omega R^2} > 1$). Since the latter is indicative of the spatial extent of the particle's field gradients, this suggests that diffusion indeed is likely to

reduce R_2*. By how much will depend on the practical conditions, including specifics of the diffusion process, and the uniformity of the particles' distribution including their potential clustering. Nevertheless, it should be realized that, due to various reasons (see below), not only R_2* but also frequency shifts, on which QSM is based, may deviate from the actual field shifts.

BIOLOGICAL ROLE OF IRON

As mentioned above, brain iron exists in various forms and in varying concentrations that change with age and disease (for review, see e.g. (33,43,75)). The ability of iron to facilitate redox reactions in which an electron is added to a substrate molecule (reduction) or extracted from a substrate (oxidation) is a key aspect of iron's immense biological significance. Important biological roles include the facilitation of neurotransmitter (e.g. dopamine) cycling, enzyme and mitochondrial function, ATP and DNA synthesis, and the generation of myelin (43,75). We will briefly discuss the various aspects of iron metabolism in the human brain.

The Proteins of Iron Metabolism

At one time there were four main proteins identified with iron metabolism in mammals; (i) hemoglobin, the major protein of the red blood cell, (ii) transferrin, a transport protein capable of binding two iron atoms and moving them through the blood and within tissues, (iii) transferrin receptor, a cell-membrane-bound-protein capable of binding transferrin and translocating it and its two iron atoms from extracellular regions to the intracellular space and (iv) ferritin, an iron-storage protein capable of storing up to 4500 iron atoms in a mineralized form. It was more or less tacitly assumed that random diffusion of iron atoms and these various proteins was a major factor determining the body's iron economy.

In the last twenty-five years or so a very large array of additional proteins involved in one aspect or another of iron metabolism and subject to intricate control mechanisms has been identified (76,77). It is likely that additional insights will result from ongoing research and these insights may lead to major revisions of current understanding. Random diffusion as a driving force has, at least in part, given way to a concept of tightly controlled (or 'chaperoned') forms of movement and chemical processes involving iron atoms.

A partial list of recently identified proteins involved with iron metabolism includes the iron regulatory protein elements IRP1 and IRP2 (78), cellular iron importers (e.g., the divalent metal transporter DMT1), exporters (ferroportin), the regulatory hormone hepcidin (79), various oxidases (e.g., ceruloplasmin and hephaestin) and reductases (DCYTB, STEAP3 see list of abbreviations for full names), etc. In addition the mitochondria have distinct iron-related molecules including iron importers (mitoferrin) and transporters (frataxin). As discussed below very recently two important additions have been made to this array of proteins involved in iron metabolism. These are the PCBP (poly(rC)-binding protein) family of iron chaperones and NCAO4, the cargo receptor mediating ferritinophagy.

The Labile Iron Pool (LIP) and the Storage Iron Pool (SIP)

In water solution both Fe^{++} and Fe^{+++} ions are liganded (solvated) by a shell of six water molecules. Fe^{+++} is highly reactive with these surrounding water molecules and almost immediately hydrolyses some waters in its coordination shells to form insoluble iron oxides and hydroxides (i.e., rust) which then precipitate. To avoid the generation of these iron precipitates the concentration of Fe^{+++} aqua-ions in the cytosol is kept at essentially zero by mechanisms described below. However, the cytosol must contain a certain level of readily reactive iron continuously available to carry out essential functions. For example, there are now hundreds of enzymes known that are produced as apoproteins in the cytosol and that require the insertion of iron-containing cofactors to function properly. There are three classes of these cofactors; heme, iron-sulfur clusters (both produced in the mitochondria) and iron aqua-ions ($Fe^{++} \cdot 6\ H_2O$ and $Fe^{+++} \cdot 6\ H_2O$) (80,81). Early on, based on biochemical and thermodynamic arguments (82), it was suggested that there is a labile iron pool (LIP) within the cytosol to support crucial metabolic processes. The LIP could be based on Fe^{++} aqua-ions and/or small molecular weight liganding molecules and should have a concentration in thevicinity of roughly 1 μM. Such a concentration would be sufficient to provide a constant supply of Fe^{++} to force the many iron-requiring enzymes in the cytosol to remain in the active, metallated form rather than the inactive apoenzyme form (83). A candidate liganding compound needs to ensure proper enzyme function and to prevent autoxidation of Fe^{++} to Fe^{+++} as well as to prevent free radical generation via the Fenton reaction. In the cytosol it would need to serve these various functions at pH = 7 and in the presence of a dissolved O_2 concentration of 2 – 5 μM (84–86). A strong candidate recently proposed as the dominant molecule in the LIP is a conjugate of Fe^{++} with the tripeptide antioxidant glutathione (87). An alternative based on a citrate molecule liganded to Fe^{++} has also been recently proposed (88).

A Storage Iron Pool (SIP) also exists within the cytoplasm of most cells. Iron storage in brain can involve iron linked to neuromelanin, lipofuscin, metallothioneins and hemosiderin as well as to ferritin. However, as storage based on ferritin is the most thoroughly studied and appears to be the most prevalent iron storage mode in the brain, only this will be discussed here. When an excess of iron in the cytoplasm is detected by the IRP proteins, a process is initiated leading to the synthesis of H and L ferritin chains. Twenty-four of these chains self-assemble into a hollow spherical protein shell with pores connecting the interior with the cytosol. Excess Fe^{++} in the LIP moves into the pores and encounters a ferroxidase site associated with the H subunits where it is oxidized to Fe^{+++}. Further, incompletely understood, steps lead to incorporation of the ferric ions into an insoluble mineralized iron oxide core capable of holding up to 4500 Fe^{+++} ions (89). When a deficit of iron in the cytosol is sensed this process is somehow reversed, the mineral is dissolved, the Fe^{+++} ions are reduced and the resulting Fe^{++} ions are released to the cytosol.

The LIP and the SIP coexist within the cytosol and their relationship is important in assessing the clinical significance and interpretation of MR images of iron-rich brain tissues. The LIP has a very small iron concentration (roughly on the order of 0.3 – 1.6 μM) (80) and is ‘below the radar’ - it is far too small to register on conventional MRI or QSM. On the other hand, the SIP in brain regions such as the basal ganglia has a much higher iron

concentration and is a prominent feature of high field MRI and QSM images. The molar SIP iron concentration in iron-rich brain regions can be estimated. On average, normal humans in the range of 30–70 years of age have roughly 200 μg iron per gram of tissue in the globus pallidus (35). Using Table 1 it is seen that this corresponds to an iron concentration of 3760 μM. In fact, this is probably a considerable underestimate in iron-rich cells as the tissue volumes studied by Hallgren and Sourander included not only cell cytoplasm but also other intracellular and extracellular regions. Also, histochemical iron staining indicates that the iron loading in these regions is not uniformly spread among the various cells but tends to be concentrated in specific cells. It is clear that iron-rich cells such as those in the globus pallidus have thousands of Fe^{+++} ions in the SIP for each Fe^{++} ion in the LIP and that MR imaging provides direct information on the SIP but not on the LIP.

A major goal of SW MRI research is to develop clinically useful information derived in part from measured brain iron concentrations. MRI has already demonstrated very clear imaging correlates of brain iron deposition with disease in a group of rare, but devastating, inherited disorders of iron metabolism (90). There is a substantial ongoing effort to accomplish this in more common neurological and psychiatric disorders such as Alzheimer's and Parkinson's diseases and depression (e.g., (91–95)). In most cases it is unclear from the MRI information alone whether the imaged brain iron effects are directly responsible for the pathology or are the result of pathological changes elsewhere that affect iron deposition in the SIP indirectly. In either case the MRI findings may be clinically relevant but this relevance would be enhanced if it was accompanied by a more or less complete understanding of the underlying iron-dependent processes but this is not currently available. Note that MRI information on brain iron reflects the status only of the SIP. However, the Fe^{+++} ions in the SIP are 'hors de combat': locked in a mineralized, insoluble, and unreactive state and unable to take part in either constructive or destructive biological processes unless released back into cytosol and the LIP.

On the other hand, the Fe^{++} ions in the LIP are continually involved with important processes such as Fenton reactions generating free radicals and the activities of possibly hundreds of iron-dependent enzymes. Thus, these ions are far too small in numbers to register on MRI but they are likely candidates for impacting both physiological and pathological brain processes. Therefore, it is to be hoped that an complete understanding of the relation between these two iron pools in the brain cytoplasm will eventually be developed as an aid in extending the clinical relevance of QSM. Two recent advances in relating the LIP and SIP involve the identification of iron metallochaperones and a process known as ferritinophagy.

Metallochaperones

When a simple metal salt (e.g., $CuSO_4$ or $FeCl_2$) is dissolved in water the metal ion becomes hydrated and diffuses freely through the solution. In cells there is a significant concentration of several different metals such as copper, iron and zinc. Many enzymes are utilized that require a particular divalent metal ion, e.g., Fe^{++}, at the active site. In many cases it is found that Cu^{++} or Zn^{++} would bind more avidly than Fe^{++} to many iron-dependent enzymes and inactivate them if Cu^{++} and Zn^{++} metal ions as well as Fe^{++} were freely available in the

cytoplasm. This and related problems can be resolved using the concept of metallochaperones. By studying the insertion of copper into an antioxidant enzyme (Cu-Zn superoxide dismutase) in yeast, it was determined that the copper ion does not diffuse freely through the cytoplasm but isinstead tightly bound to a protein that prevents it from reacting with random apoproteins and directs its insertion only into the correct substrates. This binding is sufficiently tight and the metallochaperone protein is present in sufficient concentration to assure that there is less than one 'free' copper aquaion per cell (96,97). Similar chaperone protein have also been identified for Zn^{++} (98). Thus there appears to be no pool of free copper or zinc ions in the cytoplasm.

The situation with iron is somewhat different. As was seen above, the LIP contains Fe^{++} at approximately the 1 μM level. The method by which cytosolic iron is directed to ferritin was unknown until 2008 when a human protein (PCBP1), expressed in yeast, was found to bind to both iron and ferritin and to enhance iron loading into ferritin. It therefore functions as a metallochaperone for iron (99). PCBP1 is a member of a protein family also containing PCPB2, PCPB3 and PCPB4. Each of these proteins has been demonstrated to have iron chaperone properties. Not only do these metallochaperones direct iron to ferritin but also to iron-requiring enzymes as well (80,100–106).

Ferritinophagy

Ferritin has been assumed to serve two purposes in tissues, (i) to detoxify tissues in the presence of excess iron and (ii) to store iron for future use when required for cellular needs. The discovery of iron metallochaperones was an important step toward explaining how the first function is performed but there has long been some uncertainty as to exactly how the oxidized Fe^{+++} ions in ferritin are retrieved and reduced to Fe^{++} when it is required to support cell functions (89). Autophagy is a process in which cellular components (proteins and organelles – called cargo) are enveloped within double membrane structures called autophagosomes and delivered to lysosomes for degradation and recycling of their components. It can be viewed as analogous to phagocytosis except that the object being digested has its origin internal, rather than external, to the cell, It is believed that this process may play a significant role in several important disorders including Alzheimer's, Parkinson's and Huntington's diseases (107–112).

There is now evidence indicating that the autophagy pathway has a major role in iron release from ferritin, a process called ferritinophagy. Recent studies (113,114) have identified the protein NCOA4 (nuclear receptor coactivator 4) as a cargo receptor for ferritin. This means that, in the presence of low cellular iron availability, NCOA4 binds to the ferritin H subunit, marking the ferritin molecule for transfer to a lysosome and leading to the eventual degradation of the ferritin protein shell. It has been demonstrated that NCOA4 is required for delivery of ferritin to lysosomes and that cells deficient in NCOA4 have decreased cellular iron availability. This represents a major advance in the understanding of the overall function of ferritin in cells. However, it still remains to clarify how, once the protein shell is digested, the mineralized Fe^{+++} ions are removed from the oxide core and reduced to Fe^{++} to reenter the LIP.

Implication

SW MRI has great promise in providing new approaches to imaging brain processes, particularly those involving iron. However, it is restricted to providing information on iron in the metabolically silent Storage Iron Pool. Recent developments in the cell biology of iron have indicated how an understanding of the Labile Iron Pool and its interactions with the Storage Iron Pool may aid the interpretation of SW MRI.

EFFECT OF MYELIN ON MRI CONTRAST

Myelin ensheaths most of the longer axons in the brain and serves to accelerate nerve conduction (for review, see e.g. (115)). It is formed by oligodendrocytes and consists of multiple (5–20 or more) phospholipid bilayers, which alternatingly flank intra and extra-cellular space of oligodendrocytes. Other than lipids, the bilayer contains mostly proteins and little (<20%) water whereas the opposite is true for the space between bilayers. On the millisecond-timescale of T_2 relaxation, water can be thought of as being contained in 3 distinct compartments: the axonal space, the interstitial space, and between the myelin wraps (Figure 4). The water in the latter space has long been a measurement target of methods aiming at estimating brain myelin content (116), as most hydrogen protons in the phospholipids and proteins of myelin are not directly visible with MRI. There is a substantial molecular order in the phospholipid bilayers (117), which has relevance to myelin's magnetic properties, as will be discussed below. Myelin is several-fold more abundant in WM compared to GM, because of WM's high density of myelinated fibers.

Myelin is nearly absent at birth and increases rapidly during the first 6–10 months of life (118,119). More incremental changes continue during childhood and in some regions into adolescence (119,120). In healthy adult brain, WM myelin content is about 25–35%, and it consists of about 40% water, 50% lipid and 10% protein (121,122). Abnormal myelination has been implicated with various psychiatric diseases (123), and there are a number of diseases that lead to demyelination, including amyotropic lateral sclerosis (ALS) and multiple sclerosis (MS).

Field effects and QSM of SW MRI suggest that WM is diamagnetic relative to water-like CSF (124–127), and this susceptibility shift has been attributed primarily to phospholipids in myelin. QSM-based estimates place $\Delta\chi_{myelin}$ (contribution of myelin to the susceptibility of WM) in the range of −13 to −34 ppb (66,126,128,129), not including orientation dependence of χ (see below).

As is the case with iron, the susceptibility variations introduced by myelin cause spatial variations in the magnetic field, which increase R_2*. Unfortunately, in WM, iron and myelin often colocalize (20,130,131) and can contribute with similar magnitude to R_2* (20), making it difficult to infer local myelin content from R_2* alone (Fig. 5a–c). Due to their opposing effects on tissue susceptibility however, combined analysis of R_2* and susceptibility may allow identifying the individual contributions of iron and myelin and quantify their concentration. (20,66,131,132).

Nevertheless, it has proven difficult to explain frequency and R_2* distributions in the brain based on the voxel-averaged concentrations of iron and myelin alone: across WM, substantial contrast variations have been observed that appear to reflect the orientation of major fiber bundles (133–137), although a few early studies found no clear orientation dependence (138,139). In fact, this dependence has been shown to allow prediction of fiber orientation (136). It has been attributed to the cellular structure of WM, which is highly anisotropic and makes the distribution of frequencies and their average within a voxel dependent on the structure's orientation in the static field (14). Proper interpretation of susceptibility contrast in WM requires taking the anisotropy and orientation of this microstructure into account (see next section) (14,69).

Theoretical estimates show that the structure of myelin, when modeled in very crude approximation as a set of parallel cylindrical sheaths with axis at angle θ with the field, would increase R_2* by: $\Delta R_2^* = 0.5 sin^2\theta \gamma \Delta\chi_{myelin}\, s^{-1}T^{-1}$ (69). Assuming a range of $\Delta\chi_{myelin}$ of [−13, −34] ppb (66,126,128,129), this leads to $\Delta R_2^* = [1.7-4.5]\ sin^2\theta\, s^{-1}T^{-1}$. This does not take into account effects of diffusion and orientation dependence of the susceptibility itself (see below). The experimentally determined estimates of this $sin^2\theta$ coefficient are in the range of [1–2] s^{-1} T^{-1} (134–136), somewhat lower than predicted by theory. This suggests that diffusion has a substantial effect on the R_2* of white matter. Using considerations similar as used for the iron particles above, with D~1 μm^2 ms^{-1}, R~1 μm, and $\Delta\omega$ = [8–21] s^{-1} (calculated by converting susceptibility of WM to that of pure myelin, assuming a 20% myelin volume fraction), we have $\frac{D}{\Delta\omega R^2}$ in the range of [48–125] which is much greater than one, indicating a substantial effect of diffusion on R_2*.

A further complication is that myelin's susceptibility itself has been found to be orientation dependent as well (140,141), a phenomenon that can be attributed to the orientational order of its constituent lipid molecules. Phospholipid molecules have an anisotropic susceptibility (i.e. it depends on their orientation relative to the magnetic field) (142); due to their organized arrangement in myelin's bilayers (117,143), the organized arrangement of the bilayers around the axon, and the organization of axons into fiber bundles, this anisotropy has effects on the magnetic field that are observable on the macroscopic scale (i.e. on the scale of MRI voxels) (140,141). To accurately describe the effect of anisotropic χ on the magnetization, a tensor representation of χ can be used, with $\chi_{/\!/}$ and $\chi_\perp$ as diagonal elements representing χ parallel and perpendicular to the fiber bundle respectively. MRI measurements put WM anisotropy (expressed here as $\chi_{/\!/} - \chi_\perp$) in the range of 10 to 25 ppb (141,144–148), although some of these measurements may be inaccurate due to confounding compartmental shape effects (see below). Independent estimates based on magnetic torque balance measurements (~15ppb) however fall within this range (149).

While the orientation dependencies of susceptibility and R_2* in WM complicates quantitative interpretation in terms of myelin and iron content, they may offer opportunities to map fiber orientation (136,150). As will be seen in the following, they may also offer opportunities to obtain cellular compartment specific information.

EFFECTS FROM TISSUE MICROSTRUCTURE

As hinted at above, not only the amount of substances that alter or "perturb" tissue susceptibility (e.g iron, deoxyhemoglobin and myelin) but also their microscopic distributions can affect the MRI signal. Even when susceptibility itself is isotropic, a non-uniformity at any sub-voxel spatial scale can increase R_2* and shift the frequency. The former effect can be understood by considering that perturber distribution affects field distribution, to which R_2* is sensitive (see e.g. (69)). The effect of "perturber" distribution on frequency can be understood by considering that the MRI frequency is not a faithful representation of the voxel-averaged field, in part because water proton concentration and visibility is not uniform over the voxel (e.g. where there is myelin or ferritin, there is (almost) no water); as a result, the MRI signal represents biased sampling of field. These effects need to be accounted for when calculating R_2* and susceptibility from MRI data, and when interpreting their values in terms of tissue composition.

For example, in WM, a biased sampling of the field occurs because of the compartmentalization of water around myelin, i.e. the measured frequency does not correspond to the average field in the voxel because there is little or no contribution from within the myelin sheath. An established approach (analogous to the Lorentz sphere approach discussed above) is to estimate this field is by considering average magnetic environment of a sensing proton on a water molecule (10,15); this approach has been successfully used to predict frequency shifts in biological materials such as muscle fibers, trabecular bone, and red blood cells (16,151,152)). It is based on the equivalence between averaging fields versus averaging sources that has its basis in the linearity of the Maxwell equations (10), and the incredible amount of averaging that occurs across the large number (at least 10^{14}) polarized water protons in a typical MRI voxel. For the average frequency to be reflective of the average field, substantial diffusion averaging also needs to take place, which appears a realistic assumption in brain tissue (see above, $\frac{D}{\Delta\omega R^2} \gg 1$).

Fig. 6 shows application of this concept to the simple case of uniformly distributed spherical or oriented ellipsoidal particles. Since our goal here is to estimate the effect of the particles, we ignore here (sub) atomic scale effects that are common between ^{1}H protons in pure water and ^{1}H protons in a mix of water and particles (e.g. chemical shift, dipolar coupling, and any other effects of the OH group in the water molecule or neighboring water molecules). In this simplification, the average magnetic environment seen by the proton resembles the shape of the particle: spherical particles will lead to a spherical average magnetic environment, whereas ellipsoidal particles lead to an ellipsoidal magnetic environment. This greatly simplifies estimation of the average local field at the ^{1}H nucleus, as it can be approximated by the use of one or more shape factors (see above) (10).

In WM, the magnetic environment at the sub-voxel scale can be approximated to be a continuum with cylindrical symmetry (Fig. 7, **top row**), and its effect on the resonance frequency (which we assume here to correspond to the average field) can be approximated by a cylindrical shape factor. As a result, in the axonal and interstitial space of WM, the predicted frequency shift, like R *, has an angular dependence according to

$\Delta f = 0.5 sin^2\theta \frac{\gamma}{2\pi} \Delta\chi_{myelin}\, s^{-1}$, which for the example of a fiber with $\Delta\chi_{myelin}$ = 20 *ppb* and a 90° angle with a 7 T field equates to Δ*f* ≈ 3 Hz. This seems inconsistent with (69) where, as it appears incorrectly, zero frequency shift was predicted, but analogous to (14) that uses the so-called “generalized Lorentzian” model.

The situation described above changes when considering anisotropy of the susceptibility. Computational modeling and analytical approaches suggest different shifts in different compartments in WM, specifically the spaces of axonal, extracellular, and myelin water (128,144,153), something not observed when considering only isotropic susceptibility. All these frequency shifts maintain a $sin^2\theta$ dependence (128). Again, as with the isotropic case, frequency shifts can be estimated by considering the average magnetic environment of a water proton in each compartment, and use of a corresponding shape factor (Fig. 7, **bottom row**). The latter must be a tensor in order to account for the orientation dependent nature of the magnetic environment.

The notion of compartment specific relaxation and frequency shifts has recently been confirmed experimentally (128,144). In WM, R_2* decay is triple-exponential and dependent on orientation (128,144,154), consistent with the existence of three slowly interchanging (on the R_2* time scale) water compartments (155) within and distinctly different magnetic environments. Thus, measuring the decay curve and fitting it to a sum of 3 exponentials with different frequencies would allow extraction of cellular compartment-specific information (144). For example, one could extract an estimate of the size of the myelin water compartment, which could then be interpreted as being indicative of local myelin content. This refines an approach used previously based on R_2* differences alone (156), and forms a potentially more specific alternative to myelin measurement methods based on magnetization transfer and proton density (157). As such, it may facilitate detection of myelin loss in demyelinating diseases such as MS (158). Another possible application is the use of the orientation dependence of the frequency shifts to map fiber orientation (159). Of course, compartment-specific frequency shifts are problematic for quantitative methods such as QSM and susceptibility tensor imaging and need to be accounted for (145).

SUSCEPTIBILITY CHANGES WITH DISEASE

While the potential of magnetic susceptibility contrast for the study of brain pathology had been recognized since the early days of MRI, much of the early work, performed at low field (at or below 1.5 T) focused primarily on visualizing gross changes in susceptibility due to calcifications with substantial mass, or vascular abnormalities, often associated with tumors and hemorrhages (160,161). Study of tissue iron accumulation initially was limited to the regions with highest concentration and preferentially done with T_2 contrast (38), while its specificity to iron outside these regions was rather limited (68). Transition to higher field strength and the increasing use of high-sensitivity coil arrays expanded the use of susceptibility contrast to include more subtle changes in iron and deoxyhemoglobin, and most recently, studies have started to apply SW MRI changes in brain myelin content and structure. Although many of these applications have been summarized previously (e.g. (6,18,75,162,163)), some of the major findings are highlighted below.

In the case of malignant brain tumors, SW MRI has been used to aid diagnosis and treatment based on the detection of local increases in deoxyhemoglobin and hemosiderin due to angiogenesis and vascular leakage (164–166). Additionally, SW MRI may aid in monitoring the effects of radiation therapy by detecting hemosiderin associated with micro bleeds that may result from the induced vascular damage (167). Similarly, SW may also be able to detect the microbleeds associated with traumatic brain injury, supplementing other MRI techniques in its diagnosis (168).

Both normal aging and numerous pathologies can lead to brain iron accumulation, the pattern of which may be specific to the type of pathology. Characterization of this pattern and the severity of the accumulation with SW MRI may thus help in diagnosis and possibly with monitoring of treatment. A number of neurodegenerative disorders lead to iron increases in the sub-cortical GM of the basal ganglia (34,44,169), and occasionally is constrained to specific (sub) regions. For example in CADASIL, selective accumulation has been observed in the putamen (170), whereas in Parkinson's Disease, the substantia nigra may be selectively affected (31,171). Widespread iron accumulation in cortical GM has been reported in Alzheimer's Disease (172), whereas in ALS more focal cortical accumulation has been reported (173,174). Focal iron increases also occur within or adjacent to MS lesions (175–182), and such accumulation may facilitate the detection of cortical lesions that often escape detection with other MRI contrasts (177–179,181). An interesting possibility is the detection of MS pathology based on structural changes in myelin: to the extent that these precede myelin loss, detection of such structural changes may offer an opportunity for early diagnosis in improved assessment of treatment response (144,180,183).

UNRESOLVED ISSUES

Over the last few years, tremendous progress has been made in the understanding of susceptibility contrast, in particular in WM. Additionally, much progress has been made in extracting quantitative information with potential clinical relevance, including susceptibility, R_2*, and the distribution of water between various cellular compartments. These parameters may allow quantification of biological and biophysical parameters such as tissue myelin and iron content, and the oxygenation state of tissue. Nevertheless, there a number of questions and issues that remain unresolved or not fully clarified, some of which will be discussed below.

A question that has been around for some time is the biological relevance of tissue iron and its particular distribution of the brain. Why is iron high in the basal ganglia, and what is the causal relationship with pathology? Why does iron co-localize with myelin in some fibers, but is absent in others? If iron is required for myelin generation and turnover, why does it vary so much over WM? Does some of the myelin turn over relatively rapidly? While at this point we can only speculate, it is possible that detailed mapping of iron distribution throughout the brain and over a range of pathologies may lead to some clarification in the near future. Of course, improved understanding of the relationship between LIP and SIP (see above) will be critical in this.

Another unresolved issue is the relationship between R_2* and susceptibility changes related to iron. Observed R_2* changes are generally below those predicted by theory based on a random, uniform distribution of ferritin particles. It is unclear of this reduction is entirely explained by diffusion averaging, and this is difficult to determine conclusively due to uncertainty about the uniformity of particles' distribution: clustering of particles or other types of ordering (e.g. alignment with fibers, or preference for specific cellular compartments) may substantially alter R_2*. This has relevance for quantification of tissue iron and myelin content from joint analysis of R_2* and susceptibility data. Nevertheless, a surprisingly linear relationship has been reported across GM of the basal ganglia (see above).

Puzzling also is the frequency shift attributed to the myelin water compartment for fibers perpendicular to the magnetic field in the analysis of multi-exponential relaxation in WM. Theoretical modeling suggests a strong paramagnetic frequency shift +100 ppb, whereas experimentally, a weak diamagnetic shift of about −10 ppb is observed (184). It appears therefore as if the myelin water experiences the magnetic field attributed to myelin's lipid bilayer. Full understanding is required for a confident quantification the myelin water fraction from SW data.

Lastly, it needs to be emphasized that throughout this paper, as well as the published literature, it is generally assumed that MRI signal frequency directly reports on the average local field. As indicated above, this is not necessarily true as the voxel-averaged frequency depends on the MRI-visibility of protons that contribute to the signal. T_1, T_2, and T_2* relaxation, MT, and diffusion all may affect a proton's visibility and thus its contribution to the amplitude and frequency of the average signal. This potential difference between voxel-averaged frequency and voxel-averaged field may affect the interpretation of SW MRI, as is apparent from the triple-exponential R_2* decay observed in WM. It also means that the extracted parameters may depend somewhat on the details of the MRI pulse sequence. With further research, it will become clear to what extent this issue affects quantification.

Acknowledgments

It is a pleasure to acknowledge useful discussions with Drs. SJ Kalia and M-S Ryu. JH Duyn also acknowledges the Intramural Research Program of the National Institute of Neurological Disorders and Stroke for support.

ABBREVIATIONS

ALS	Amyotrophic Lateral Sclerosis
BOLD	Blood Oxygen Level Dependent
CADASIL	Cerebral Autosomal Dominant Arteriopathy with Subcortical Infarcts and Leukoencephalopathy
CBV	Cerebral Blood Volume
DAB	Diaminobenzidine
DCYTB	Duodenal Cytochrome B

DMT	Divalent Metal Transporter
GM	Grey Matter
IRP	Iron Regulatory Protein
LIP	Labile Iron Pool
MS	Multiple Sclerosis
NCOA	Nuclear Receptor Coactivator
PCBP	Poly(rC) Binding Protein
QSM	Quantitative Susceptibility Mapping
SIP	Storage Iron Pool
STEAP	Six-Transmembrane Epithelial Antigen of the Prostate family
SW	Susceptibility Weighted
WM	White Matter

References

1. Li TQ, Yao B, van Gelderen P, Merkle H, Koretsky A, Duyn JH. Cortical Architecture of the Human Hippocampus. Proc Ann Meeting ISMRM. 2008:2219.
2. Duyn JH, van Gelderen P, Li TQ, de Zwart JA, Koretsky AP, Fukunaga M. High-field MRI of brain cortical substructure based on signal phase. Proceedings of the National Academy of Sciences of the United States of America. 2007; 104(28):11796–11801. [PubMed: 17586684]
3. Ogawa S, Tank DW, Menon R, Ellermann JM, Kim SG, Merkle H, Ugurbil K. Intrinsic signal changes accompanying sensory stimulation: functional brain mapping with magnetic resonance imaging. Proceedings of the National Academy of Sciences of the United States of America. 1992; 89(13):5951–5955. [PubMed: 1631079]
4. Haacke EM, Cheng NY, House MJ, Liu Q, Neelavalli J, Ogg RJ, Khan A, Ayaz M, Kirsch W, Obenaus A. Imaging iron stores in the brain using magnetic resonance imaging. Magn Reson Imaging. 2005; 23(1):1–25. [PubMed: 15733784]
5. Reichenbach JR. The future of susceptibility contrast for assessment of anatomy and function. NeuroImage. 2012; 62(2):1311–1315. [PubMed: 22245644]
6. Liu C, Li W, Tong KA, Yeom KW, Kuzminski S. Susceptibility-weighted imaging and quantitative susceptibility mapping in the brain. Journal of magnetic resonance imaging: JMRI. 2015; 42(1):23–41. [PubMed: 25270052]
7. Haacke EM, Liu S, Buch S, Zheng W, Wu D, Ye Y. Quantitative susceptibility mapping: current status and future directions. Magn Reson Imaging. 2015; 33(1):1–25. [PubMed: 25267705]
8. Schenck JF. The role of magnetic susceptibility in magnetic resonance imaging: MRI magnetic compatibility of the first and second kinds. Medical physics. 1996; 23(6):815–850. [PubMed: 8798169]
9. Atlas SW, Grossman RI, Hackney DB, Gomori JM, Campagna N, Goldberg HI, Bilaniuk LT, Zimmerman RA. Calcified intracranial lesions: detection with gradient-echo-acquisition rapid MR imaging. AJR American journal of roentgenology. 1988; 150(6):1383–1389. [PubMed: 3259383]
10. Durrant CJ, Hertzberg MP, Kuchel PW. Magnetic susceptibility: Further insights into macroscopic and miroscopic fields and the sphere of lorentz. Concept Magn Reson A. 2003; 18A(1):72–95.
11. Chu SC, Xu Y, Balschi JA, Springer CS Jr. Bulk magnetic susceptibility shifts in NMR studies of compartmentalized samples: use of paramagnetic reagents. Magnetic resonance in medicine:

official journal of the Society of Magnetic Resonance in Medicine/Society of Magnetic Resonance in Medicine. 1990; 13(2):239–262.

12. Wang Y, Liu T. Quantitative susceptibility mapping (QSM): Decoding MRI data for a tissue magnetic biomarker. Magnetic resonance in medicine: official journal of the Society of Magnetic Resonance in Medicine/Society of Magnetic Resonance in Medicine. 2014
13. Reichenbach JR, Schweser F, Serres B, Deistung A. Quantitative Susceptibility Mapping: Concepts and Applications. Clinical neuroradiology. 2015; 25(Suppl 2):225–230.
14. He X, Yablonskiy DA. Biophysical mechanisms of phase contrast in gradient echo MRI. Proceedings of the National Academy of Sciences of the United States of America. 2009; 106(32): 13558–13563. [PubMed: 19628691]
15. Duyn JH, Barbara TM. Sphere of Lorentz and demagnetization factors in white matter. Magnetic resonance in medicine: official journal of the Society of Magnetic Resonance in Medicine/Society of Magnetic Resonance in Medicine. 2014; 72(1):1–3.
16. Wolber J, Cherubini A, Leach MO, Bifone A. Hyperpolarized 129Xe NMR as a probe for blood oxygenation. Magnetic resonance in medicine: official journal of the Society of Magnetic Resonance in Medicine/Society of Magnetic Resonance in Medicine. 2000; 43(4):491–496.
17. Haacke EM, Xu Y, Cheng YC, Reichenbach JR. Susceptibility weighted imaging (SWI). Magnetic resonance in medicine: official journal of the Society of Magnetic Resonance in Medicine/Society of Magnetic Resonance in Medicine. 2004; 52(3):612–618.
18. Mittal S, Wu Z, Neelavalli J, Haacke EM. Susceptibility-weighted imaging: technical aspects and clinical applications, part 2. AJNR American journal of neuroradiology. 2009; 30(2):232–252. [PubMed: 19131406]
19. Cohen-Adad J, Polimeni JR, Helmer KG, Benner T, McNab JA, Wald LL, Rosen BR, Mainero C. T(2)* mapping and B(0) orientation-dependence at 7 T reveal cyto- and myeloarchitecture organization of the human cortex. NeuroImage. 2012; 60(2):1006–1014. [PubMed: 22270354]
20. Fukunaga M, Li TQ, van Gelderen P, de Zwart JA, Shmueli K, Yao B, Lee J, Maric D, Aronova MA, Zhang G, Leapman RD, Schenck JF, Merkle H, Duyn JH. Layer-specific variation of iron content in cerebral cortex as a source of MRI contrast. Proceedings of the National Academy of Sciences of the United States of America. 2010; 107(8):3834–3839. [PubMed: 20133720]
21. Marques JP, van der Zwaag W, Granziera C, Krueger G, Gruetter R. Cerebellar cortical layers: in vivo visualization with structural high-field-strength MR imaging. Radiology. 2010; 254(3):942–948. [PubMed: 20177104]
22. Thomas BP, Welch EB, Niederhauser BD, Whetsell WO Jr, Anderson AW, Gore JC, Avison MJ, Creasy JL. High-resolution 7T MRI of the human hippocampus in vivo. Journal of magnetic resonance imaging: JMRI. 2008; 28(5):1266–1272. [PubMed: 18972336]
23. Cho ZH, Han JY, Hwang SI, Kim DS, Kim KN, Kim NB, Kim SJ, Chi JG, Park CW, Kim YB. Quantitative analysis of the hippocampus using images obtained from 7. 0 T. MRI NeuroImage. 2010; 49(3):2134–2140. [PubMed: 19909820]
24. Augustinack JC, Huber KE, Stevens AA, Roy M, Frosch MP, van der Kouwe AJ, Wald LL, Van Leemput K, McKee AC, Fischl B. Alzheimer's Disease Neuroimaging I. Predicting the location of human perirhinal cortex, Brodmann's area 35, from MRI. NeuroImage. 2013; 64:32–42. [PubMed: 22960087]
25. Vertinsky AT, Coenen VA, Lang DJ, Kolind S, Honey CR, Li D, Rauscher A. Localization of the subthalamic nucleus: optimization with susceptibility-weighted phase MR imaging. AJNR American journal of neuroradiology. 2009; 30(9):1717–1724. [PubMed: 19509077]
26. Kerl HU, Gerigk L, Huck S, Al-Zghloul M, Groden C, Nolte IS. Visualisation of the zona incerta for deep brain stimulation at 3. 0 Tesla. Clinical neuroradiology. 2012; 22(1):55–68. [PubMed: 22349435]
27. Abosch A, Yacoub E, Ugurbil K, Harel N. An assessment of current brain targets for deep brain stimulation surgery with susceptibility-weighted imaging at 7 tesla. Neurosurgery. 2010; 67(6): 1745–1756. discussion 1756. [PubMed: 21107206]
28. Walsh AJ, Wilman AH. Susceptibility phase imaging with comparison to R2 mapping of iron-rich deep grey matter. NeuroImage. 2011; 57(2):452–461. [PubMed: 21513807]

29. Nolte IS, Gerigk L, Al-Zghloul M, Groden C, Kerl HU. Visualization of the internal globus pallidus: sequence and orientation for deep brain stimulation using a standard installation protocol at 3. 0 Tesla. Acta neurochirurgica. 2012; 154(3):481–494. [PubMed: 22167532]
30. Lotfipour AK, Wharton S, Schwarz ST, Gontu V, Schafer A, Peters AM, Bowtell RW, Auer DP, Gowland PA, Bajaj NP. High resolution magnetic susceptibility mapping of the substantia nigra in Parkinson's disease. Journal of magnetic resonance imaging: JMRI. 2012; 35(1):48–55. [PubMed: 21987471]
31. Cho ZH, Oh SH, Kim JM, Park SY, Kwon DH, Jeong HJ, Kim YB, Chi JG, Park CW, Huston J 3rd, Lee KH, Jeon BS. Direct visualization of Parkinson's disease by in vivo human brain imaging using 7. 0T magnetic resonance imaging. Movement disorders: official journal of the Movement Disorder Society. 2011; 26(4):713–718. [PubMed: 21506148]
32. Di Ieva A, Lam T, Alcaide-Leon P, Bharatha A, Montanera W, Cusimano MD. Magnetic resonance susceptibility weighted imaging in neurosurgery: current applications and future perspectives. Journal of neurosurgery. 2015:1–13.
33. Schenck JF, Zimmerman EA. High-field magnetic resonance imaging of brain iron: birth of a biomarker? NMR in biomedicine. 2004; 17(7):433–445. [PubMed: 15523705]
34. Schipper HM. Neurodegeneration with brain iron accumulation - clinical syndromes and neuroimaging. Biochimica et biophysica acta. 2012; 1822(3):350–360. [PubMed: 21782937]
35. Hallgren B, Sourander P. The effect of age on the non-haemin iron in the human brain. J Neurochem. 1958; 3(1):41–51. [PubMed: 13611557]
36. Hallgren B, Sourander P. The non-haemin iron in the cerebral cortex in Alzheimer's disease. J Neurochem. 1960; 5:307–310. [PubMed: 14399117]
37. Morris CM, Candy JM, Oakley AE, Bloxham CA, Edwardson JA. Histochemical distribution of non-haem iron in the human brain. Acta Anat (Basel). 1992; 144(3):235–257. [PubMed: 1529678]
38. Drayer B, Burger P, Darwin R, Riederer S, Herfkens R, Johnson GA. MRI of brain iron. Am J Roentgenol. 1986; 147(1):103–110. [PubMed: 3487201]
39. Connor JR, Menzies SL, St Martin SM, Mufson EJ. Cellular distribution of transferrin, ferritin, and iron in normal and aged human brains. J Neurosci Res. 1990; 27(4):595–611. [PubMed: 2079720]
40. Rutledge JN, Hilal SK, Silver AJ, Defendini R, Fahn S. Study of movement disorders and brain iron by MR. AJR American journal of roentgenology. 1987; 149(2):365–379. [PubMed: 2440291]
41. LeVine SM, Macklin WB. Iron-enriched oligodendrocytes: a reexamination of their spatial distribution. J Neurosci Res. 1990; 26(4):508–512. [PubMed: 1700140]
42. Miyajima H. Aceruloplasminemia. Neuropathology: official journal of the Japanese Society of Neuropathology. 2015; 35(1):83–90. [PubMed: 25168455]
43. Burdo JR, Connor JR. Brain iron uptake and homeostatic mechanisms: an overview. Biometals. 2003; 16(1):63–75. [PubMed: 12572665]
44. Ward RJ, Zucca FA, Duyn JH, Crichton RR, Zecca L. The role of iron in brain ageing and neurodegenerative disorders. The Lancet Neurology. 2014; 13(10):1045–1060. [PubMed: 25231526]
45. Pal PK, Samii A, Calne DB. Manganese neurotoxicity: a review of clinical features, imaging and pathology. Neurotoxicology. 1999; 20(2–3):227–238. [PubMed: 10385886]
46. McDonald RJ, McDonald JS, Kallmes DF, Jentoft ME, Murray DL, Thielen KR, Williamson EE, Eckel LJ. Intracranial Gadolinium Deposition after Contrast-enhanced MR Imaging. Radiology. 2015; 275(3):772–782. [PubMed: 25742194]
47. Connor JR. Pathophysiology of restless legs syndrome: evidence for iron involvement. Curr Neurol Neurosci Rep. 2008; 8(2):162–166. [PubMed: 18460286]
48. Ogawa S, Lee TM. Magnetic resonance imaging of blood vessels at high fields: in vivo and in vitro measurements and image simulation. Magnetic resonance in medicine: official journal of the Society of Magnetic Resonance in Medicine/Society of Magnetic Resonance in Medicine. 1990; 16(1):9–18.
49. Schenck JF. Health and physiological effects of human exposure to whole-body four-tesla magnetic fields during MRI. Ann N Y Acad Sci. 1992; 649:285–301. [PubMed: 1580500]

50. Ogawa S, Lee TM, Kay AR, Tank DW. Brain magnetic resonance imaging with contrast dependent on blood oxygenation. Proceedings of the National Academy of Sciences of the United States of America. 1990; 87(24):9868–9872. [PubMed: 2124706]
51. He X, Yablonskiy DA. Quantitative BOLD: mapping of human cerebral deoxygenated blood volume and oxygen extraction fraction: default state. Magnetic resonance in medicine: official journal of the Society of Magnetic Resonance in Medicine/Society of Magnetic Resonance in Medicine. 2007; 57(1):115–126.
52. Christen T, Schmiedeskamp H, Straka M, Bammer R, Zaharchuk G. Measuring brain oxygenation in humans using a multiparametric quantitative blood oxygenation level dependent MRI approach. Magnetic resonance in medicine: official journal of the Society of Magnetic Resonance in Medicine/Society of Magnetic Resonance in Medicine. 2012; 68(3):905–911.
53. Fan AP, Bilgic B, Gagnon L, Witzel T, Bhat H, Rosen BR, Adalsteinsson E. Quantitative oxygenation venography from MRI phase. Magnetic resonance in medicine: official journal of the Society of Magnetic Resonance in Medicine/Society of Magnetic Resonance in Medicine. 2014; 72(1):149–159.
54. Reichenbach JR, Venkatesan R, Schillinger DJ, Kido DK, Haacke EM. Small vessels in the human brain: MR venography with deoxyhemoglobin as an intrinsic contrast agent. Radiology. 1997; 204(1):272–277. [PubMed: 9205259]
55. Lee J, Hirano Y, Fukunaga M, Silva AC, Duyn JH. On the contribution of deoxy-hemoglobin to MRI gray-white matter phase contrast at high field. NeuroImage. 2010; 49(1):193–198. [PubMed: 19619663]
56. Duvernoy HM, Delon S, Vannson JL. Cortical blood vessels of the human brain. Brain Res Bull. 1981; 7(5):519–579. [PubMed: 7317796]
57. Weber B, Keller AL, Reichold J, Logothetis NK. The microvascular system of the striate and extrastriate visual cortex of the macaque. Cerebral cortex. 2008; 18(10):2318–2330. [PubMed: 18222935]
58. Haacke EM, Beggs CB, Habib C. The role of venous abnormalities in neurological disease. Rev Recent Clin Trials. 2012; 7(2):100–116. [PubMed: 22338620]
59. Kou Z, Wu Z, Tong KA, Holshouser B, Benson RR, Hu J, Haacke EM. The role of advanced MR imaging findings as biomarkers of traumatic brain injury. The Journal of head trauma rehabilitation. 2010; 25(4):267–282. [PubMed: 20611045]
60. Brooks RA, Vymazal J, Goldfarb RB, Bulte JW, Aisen P. Relaxometry and magnetometry of ferritin. Magnetic resonance in medicine: official journal of the Society of Magnetic Resonance in Medicine/Society of Magnetic Resonance in Medicine. 1998; 40(2):227–235.
61. Zheng W, Nichol H, Liu S, Cheng YC, Haacke EM. Measuring iron in the brain using quantitative susceptibility mapping and X-ray fluorescence imaging. NeuroImage. 2013; 78:68–74. [PubMed: 23591072]
62. Langkammer C, Schweser F, Krebs N, Deistung A, Goessler W, Scheurer E, Sommer K, Reishofer G, Yen K, Fazekas F, Ropele S, Reichenbach JR. Quantitative susceptibility mapping (QSM) as a means to measure brain iron? A post mortem validation study. NeuroImage. 2012; 62(3):1593–1599. [PubMed: 22634862]
63. Shmueli K, de Zwart JA, van Gelderen P, Li TQ, Dodd SJ, Duyn JH. Magnetic susceptibility mapping of brain tissue in vivo using MRI phase data. Magnetic resonance in medicine: official journal of the Society of Magnetic Resonance in Medicine/Society of Magnetic Resonance in Medicine. 2009; 62(6):1510–1522.
64. Wharton S, Bowtell R. Whole-brain susceptibility mapping at high field: a comparison of multiple- and single-orientation methods. NeuroImage. 2010; 53(2):515–525. [PubMed: 20615474]
65. Schweser F, Deistung A, Lehr BW, Reichenbach JR. Quantitative imaging of intrinsic magnetic tissue properties using MRI signal phase: an approach to in vivo brain iron metabolism? NeuroImage. 2011; 54(4):2789–2807. [PubMed: 21040794]
66. Stuber C, Morawski M, Schafer A, Labadie C, Wahnert M, Leuze C, Streicher M, Barapatre N, Reimann K, Geyer S, Spemann D, Turner R. Myelin and iron concentration in the human brain: a quantitative study of MRI contrast. NeuroImage. 2014; 93(Pt 1):95–106. [PubMed: 24607447]

67. Bilgic B, Pfefferbaum A, Rohlfing T, Sullivan EV, Adalsteinsson E. MRI estimates of brain iron concentration in normal aging using quantitative susceptibility mapping. NeuroImage. 2012; 59(3):2625–2635. [PubMed: 21925274]
68. Ordidge RJ, Gorell JM, Deniau JC, Knight RA, Helpern JA. Assessment of relative brain iron concentrations using T2-weighted and T2*-weighted MRI at 3 Tesla. Magnetic resonance in medicine: official journal of the Society of Magnetic Resonance in Medicine/Society of Magnetic Resonance in Medicine. 1994; 32(3):335–341.
69. Yablonskiy DA, Haacke EM. Theory of NMR signal behavior in magnetically inhomogeneous tissues: the static dephasing regime. Magnetic resonance in medicine: official journal of the Society of Magnetic Resonance in Medicine/Society of Magnetic Resonance in Medicine. 1994; 32(6):749–763.
70. Yao B, Li TQ, van Gelderen P, Shmueli K, de Zwart JA, Duyn JH. Susceptibility contrast in high field MRI of human brain as a function of tissue iron content. NeuroImage. 2009; 44(4):1259–1266. [PubMed: 19027861]
71. Gelman N, Gorell JM, Barker PB, Savage RM, Spickler EM, Windham JP, Knight RA. MR imaging of human brain at 3. 0 T: preliminary report on transverse relaxation rates and relation to estimated iron content. Radiology. 1999; 210(3):759–767. [PubMed: 10207479]
72. Deistung A, Schafer A, Schweser F, Biedermann U, Turner R, Reichenbach JR. Toward in vivo histology: a comparison of quantitative susceptibility mapping (QSM) with magnitude-, phase-, and R2*-imaging at ultra-high magnetic field strength. NeuroImage. 2013; 65:299–314. [PubMed: 23036448]
73. Sun H, Walsh AJ, Lebel RM, Blevins G, Catz I, Lu JQ, Johnson ES, Emery DJ, Warren KG, Wilman AH. Validation of quantitative susceptibility mapping with Perls' iron staining for subcortical gray matter. NeuroImage. 2015; 105:486–492. [PubMed: 25462797]
74. Muller RN, Gillis P, Moiny F, Roch A. Transverse relaxivity of particulate MRI contrast media: from theories to experiments. Magnetic resonance in medicine: official journal of the Society of Magnetic Resonance in Medicine/Society of Magnetic Resonance in Medicine. 1991; 22(2):178–182. discussion 195–176.
75. Dusek P, Dezortova M, Wuerfel J. Imaging of iron. International review of neurobiology. 2013; 110:195–239. [PubMed: 24209440]
76. Crichton, RR., Boelaert, JR. Inorganic biochemistry of iron metabolism: from molecular mechanisms to clinical consequences. Chichester; New York: Wiley; 2001. p. xxiip. 326316 p. of plates p
77. Testa, U. Proteins of iron metabolism. Boca Raton, Fla: CRC Press; 2002. p. 559
78. Anderson CP, Shen M, Eisenstein RS, Leibold EA. Mammalian iron metabolism and its control by iron regulatory proteins. Biochim Biophys Acta. 2012; 1823(9):1468–1483. [PubMed: 22610083]
79. Du F, Qian ZM, Luo Q, Yung WH, Ke Y. Hepcidin Suppresses Brain Iron Accumulation by Downregulating Iron Transport Proteins in Iron-Overloaded Rats. Mol Neurobiol. 2015; 52(1): 101–114. [PubMed: 25115800]
80. Philpott CC, Ryu MS. Special delivery: distributing iron in the cytosol of mammalian cells. Front Pharmacol. 2014; 5:173. [PubMed: 25101000]
81. Waldron KJ, Rutherford JC, Ford D, Robinson NJ. Metalloproteins and metal sensing. Nature. 2009; 460(7257):823–830. [PubMed: 19675642]
82. Williams RJ. Free manganese (II) and iron (II) cations can act as intracellular cell controls. FEBS Lett. 1982; 140(1):3–10. [PubMed: 7084455]
83. Hider RC, Kong X. Iron speciation in the cytosol: an overview. Dalton Trans. 2013; 42(9):3220–3229. [PubMed: 23232973]
84. Halliwell, B., Gutteridge, JMC. Free radicals in biology and medicine. New York, NY: Oxford University Press; 2015. pages cm p
85. Kosman DJ. Iron metabolism in aerobes: managing ferric iron hydrolysis and ferrous iron autoxidation. Coord Chem Rev. 2013; 257(1):210–217. [PubMed: 23264695]
86. Pierre JL, Fontecave M, Crichton RR. Chemistry for an essential biological process: the reduction of ferric iron. Biometals. 2002; 15(4):341–346. [PubMed: 12405527]

87. Hider RC, Kong XL. Glutathione: a key component of the cytoplasmic labile iron pool. Biometals. 2011; 24(6):1179–1187. [PubMed: 21769609]

88. Shvartsman M, Cabantchik IZ. Intracellular iron trafficking: role of cytosolic ligands. Biometals. 2012; 25(4):711–723. [PubMed: 22350471]

89. Theil, EC. Ferritin. In: Bertini, I.Gray, HB.Stiefel, EI., Valentine, JS., editors. Biological inorganic chemistry: structure and reactivity. Sausalito, Calif: University Science Books; 2007. p. 144-150.

90. McNeill A, Birchall D, Hayflick SJ, Gregory A, Schenck JF, Zimmerman EA, Shang H, Miyajima H, Chinnery PF. T2* and FSE MRI distinguishes four subtypes of neurodegeneration with brain iron accumulation. Neurology. 2008; 70(18):1614–1619. [PubMed: 18443312]

91. Friedman A, Galazka-Friedman J, Koziorowski D. Iron as a cause of Parkinson disease - a myth or a well established hypothesis? Parkinsonism Relat Disord. 2009; 15(Suppl 3):S212–214. [PubMed: 20082993]

92. Hare D, Ayton S, Bush A, Lei P. A delicate balance: Iron metabolism and diseases of the brain. Front Aging Neurosci. 2013; 5:34. [PubMed: 23874300]

93. Rouault TA. Iron metabolism in the CNS: implications for neurodegenerative diseases. Nat Rev Neurosci. 2013; 14(8):551–564. [PubMed: 23820773]

94. White AR, Kanninen KM, Crouch PJ. Editorial: Metals and neurodegeneration: restoring the balance. Front Aging Neurosci. 2015; 7:127. [PubMed: 26191002]

95. Wong BX, Duce JA. The iron regulatory capability of the major protein participants in prevalent neurodegenerative disorders. Front Pharmacol. 2014; 5:81. [PubMed: 24795635]

96. Finney LA, O'Halloran TV. Transition metal speciation in the cell: insights from the chemistry of metal ion receptors. Science. 2003; 300(5621):931–936. [PubMed: 12738850]

97. Rae TD, Schmidt PJ, Pufahl RA, Culotta VC, O'Halloran TV. Undetectable intracellular free copper: the requirement of a copper chaperone for superoxide dismutase. Science. 1999; 284(5415):805–808. [PubMed: 10221913]

98. Outten CE, O'Halloran TV. Femtomolar sensitivity of metalloregulatory proteins controlling zinc homeostasis. Science. 2001; 292(5526):2488–2492. [PubMed: 11397910]

99. Shi H, Bencze KZ, Stemmler TL, Philpott CC. A cytosolic iron chaperone that delivers iron to ferritin. Science. 2008; 320(5880):1207–1210. [PubMed: 18511687]

100. Frey AG, Nandal A, Park JH, Smith PM, Yabe T, Ryu MS, Ghosh MC, Lee J, Rouault TA, Park MH, Philpott CC. Iron chaperones PCBP1 and PCBP2 mediate the metallation of the dinuclear iron enzyme deoxyhypusine hydroxylase. Proc Natl Acad Sci U S A. 2014; 111(22):8031–8036. [PubMed: 24843120]

101. Jhurry ND, Chakrabarti M, McCormick SP, Gohil VM, Lindahl PA. Mossbauer study and modeling of iron import and trafficking in human jurkat cells. Biochemistry. 2013; 52(45):7926–7942. [PubMed: 24180611]

102. Leidgens S, Bullough KZ, Shi H, Li F, Shakoury-Elizeh M, Yabe T, Subramanian P, Hsu E, Natarajan N, Nandal A, Stemmler TL, Philpott CC. Each member of the poly-r(C)-binding protein 1 (PCBP) family exhibits iron chaperone activity toward ferritin. J Biol Chem. 2013; 288(24):17791–17802. [PubMed: 23640898]

103. Nandal A, Ruiz JC, Subramanian P, Ghimire-Rijal S, Sinnamon RA, Stemmler TL, Bruick RK, Philpott CC. Activation of the HIF prolyl hydroxylase by the iron chaperones PCBP1 and PCBP2. Cell Metab. 2011; 14(5):647–657. [PubMed: 22055506]

104. Philpott C. Bioinorganic chemistry: Getting a grip on iron. Nat Chem Biol. 2010; 6(8):568–570. [PubMed: 20644542]

105. Philpott CC. Coming into view: eukaryotic iron chaperones and intracellular iron delivery. J Biol Chem. 2012; 287(17):13518–13523. [PubMed: 22389494]

106. Philpott CC. Pumping iron. Elife. 2014; 3:e03997. [PubMed: 25128012]

107. Biasiotto G, Di Lorenzo D, Archetti S, Zanella I. Iron and Neurodegeneration: Is Ferritinophagy the Link? Mol Neurobiol. 2015

108. Dowdle WE, Nyfeler B, Nagel J, Elling RA, Liu S, Triantafellow E, Menon S, Wang Z, Honda A, Pardee G, Cantwell J, Luu C, Cornella-Taracido I, Harrington E, Fekkes P, Lei H, Fang Q, Digan ME, Burdick D, Powers AF, Helliwell SB, D'Aquin S, Bastien J, Wang H, Wiederschain D, Kuerth J, Bergman P, Schwalb D, Thomas J, Ugwonali S, Harbinski F, Tallarico J, Wilson CJ,

Myer VE, Porter JA, Bussiere DE, Finan PM, Labow MA, Mao X, Hamann LG, Manning BD, Valdez RA, Nicholson T, Schirle M, Knapp MS, Keaney EP, Murphy LO. Selective VPS34 inhibitor blocks autophagy and uncovers a role for NCOA4 in ferritin degradation and iron homeostasis in vivo. Nat Cell Biol. 2014; 16(11):1069–1079. [PubMed: 25327288]

109. Goodall M, Thorburn A. Identifying specific receptors for cargo-mediated autophagy. Cell Res. 2014; 24(7):783–784. [PubMed: 24797431]
110. Kaur J, Debnath J. Autophagy at the crossroads of catabolism and anabolism. Nat Rev Mol Cell Biol. 2015; 16(8):461–472. [PubMed: 26177004]
111. Krishan S, Jansson PJ, Gutierrez E, Lane DJ, Richardson D, Sahni S. Iron Metabolism and Autophagy: A Poorly Explored Relationship That Has Important Consequences for Health and Disease. Nagoya J Med Sci. 2015; 77(1–2):1–6. [PubMed: 25797965]
112. Ochaba J, Lukacsovich T, Csikos G, Zheng S, Margulis J, Salazar L, Mao K, Lau AL, Yeung SY, Humbert S, Saudou F, Klionsky DJ, Finkbeiner S, Zeitlin SO, Marsh JL, Housman DE, Thompson LM, Steffan JS. Potential function for the Huntingtin protein as a scaffold for selective autophagy. Proc Natl Acad Sci U S A. 2014; 111(47):16889–16894. [PubMed: 25385587]
113. Mancias JD, Pontano Vaites L, Nissim S, Biancur DE, Kim AJ, Wang X, Liu Y, Goessling W, Kimmelman AC, Harper JW. Ferritinophagy via NCOA4 is required for erythropoiesis and is regulated by iron dependent HERC2-mediated proteolysis. Elife. 2015; 4
114. Mancias JD, Wang X, Gygi SP, Harper JW, Kimmelman AC. Quantitative proteomics identifies NCOA4 as the cargo receptor mediating ferritinophagy. Nature. 2014; 509(7498):105–109. [PubMed: 24695223]
115. Hildebrand C, Remahl S, Persson H, Bjartmar C. Myelinated nerve fibres in the CNS. Prog Neurobiol. 1993; 40(3):319–384. [PubMed: 8441812]
116. MacKay AL, Vavasour IM, Rauscher A, Kolind SH, Madler B, Moore GR, Traboulsee AL, Li DK, Laule C. MR relaxation in multiple sclerosis. Neuroimaging clinics of North America. 2009; 19(1):1–26. [PubMed: 19064196]
117. Bloom M, Burnell EE, MacKay AL, Nichol CP, Valic MI, Weeks G. Fatty acyl chain order in lecithin model membranes determined from proton magnetic resonance. Biochemistry. 1978; 17(26):5750–5762. [PubMed: 581557]
118. Paus T, Collins DL, Evans AC, Leonard G, Pike B, Zijdenbos A. Maturation of white matter in the human brain: a review of magnetic resonance studies. Brain Res Bull. 2001; 54(3):255–266. [PubMed: 11287130]
119. Dean DC 3rd, O'Muircheartaigh J, Dirks H, Waskiewicz N, Walker L, Doernberg E, Piryatinsky I, Deoni SC. Characterizing longitudinal white matter development during early childhood. Brain Struct Funct. 2015; 220(4):1921–1933. [PubMed: 24710623]
120. Deoni SC, Dean DC 3rd, Remer J, Dirks H, O'Muircheartaigh J. Cortical maturation and myelination in healthy toddlers and young children. NeuroImage. 2015; 115:147–161. [PubMed: 25944614]
121. O'Brien JS, Sampson EL. Lipid composition of the normal human brain: gray matter, white matter, and myelin. J Lipid Res. 1965; 6(4):537–544. [PubMed: 5865382]
122. Horch RA, Gore JC, Does MD. Origins of the ultrashort-T2 1H NMR signals in myelinated nerve: a direct measure of myelin content? Magnetic resonance in medicine: official journal of the Society of Magnetic Resonance in Medicine/Society of Magnetic Resonance in Medicine. 2011; 66(1):24–31.
123. Paus T, Keshavan M, Giedd JN. Why do many psychiatric disorders emerge during adolescence? Nat Rev Neurosci. 2008; 9(12):947–957. [PubMed: 19002191]
124. Zhong K, Ernst T, Buchthal S, Speck O, Anderson L, Chang L. Phase contrast imaging in neonates. NeuroImage. 2011; 55(3):1068–1072. [PubMed: 21232619]
125. Lodygensky GA, Marques JP, Maddage R, Perroud E, Sizonenko SV, Huppi PS, Gruetter R. In vivo assessment of myelination by phase imaging at high magnetic field. NeuroImage. 2012; 59(3):1979–1987. [PubMed: 21985911]

126. Lee J, Shmueli K, Kang BT, Yao B, Fukunaga M, van Gelderen P, Palumbo S, Bosetti F, Silva AC, Duyn JH. The contribution of myelin to magnetic susceptibility-weighted contrasts in high-field MRI of the brain. NeuroImage. 2012; 59(4):3967–3975. [PubMed: 22056461]

127. Liu C, Li W, Johnson GA, Wu B. High-field (9. 4 T) MRI of brain dysmyelination by quantitative mapping of magnetic susceptibility. NeuroImage. 2011; 56(3):930–938. [PubMed: 21320606]

128. Wharton S, Bowtell R. Fiber orientation-dependent white matter contrast in gradient echo MRI. Proceedings of the National Academy of Sciences of the United States of America. 2012; 109(45):18559–18564. [PubMed: 23091011]

129. Schweser F, Sommer K, Deistung A, Reichenbach JR. Quantitative susceptibility mapping for investigating subtle susceptibility variations in the human brain. NeuroImage. 2012

130. LeVine SM. Oligodendrocytes and myelin sheaths in normal, quaking and shiverer brains are enriched in iron. J Neurosci Res. 1991; 29(3):413–419. [PubMed: 1920537]

131. Fukunaga M, Li TQ, van Gelderen P, de Zwart JA, Shmueli K, Yao B, Lee J, Maric D, Aronova MA, Zhang GF, Leapman RD, Schenck JF, Merkle H, Duyn JH. Layer-specific variation of iron content in cerebral cortex as a source of MRI contrast. Proceedings of the National Academy of Sciences of the United States of America. 2010; 107(8):3834–3839. [PubMed: 20133720]

132. Schweser F, Deistung A, Lehr BW, Reichenbach JR. Differentiation between diamagnetic and paramagnetic cerebral lesions based on magnetic susceptibility mapping. Medical physics. 2010; 37(10):5165–5178. [PubMed: 21089750]

133. Wiggins CJ, Gudmundsdottir V, Le Bihan D, Lebon V, Chaumeil M. Orientation Dependence of White Matter T2* Contrast at 7T: A Direct Demonstration. Proc Soc Magn Magn Reson Med. 2008:237.

134. Bender B, Klose U. The in vivo influence of white matter fiber orientation towards B(0) on T2* in the human brain. NMR in biomedicine. 2010; 23(9):1071–1076. [PubMed: 20665897]

135. Denk C, Hernandez Torres E, MacKay A, Rauscher A. The influence of white matter fibre orientation on MR signal phase and decay. NMR in biomedicine. 2011; 24(3):246–252. [PubMed: 21404336]

136. Lee J, van Gelderen P, Kuo LW, Merkle H, Silva AC, Duyn JH. T2*-based fiber orientation mapping. NeuroImage. 2011; 57(1):225–234. [PubMed: 21549203]

137. Sati P, Silva AC, van Gelderen P, Gaitan MI, Wohler JE, Jacobson S, Duyn JH, Reich DS. In vivo quantification of T(2) anisotropy in white matter fibers in marmoset monkeys. NeuroImage. 2012; 59(2):979–985. [PubMed: 21906687]

138. Cherubini A, Peran P, Hagberg GE, Varsi AE, Luccichenti G, Caltagirone C, Sabatini U, Spalletta G. Characterization of white matter fiber bundles with T2* relaxometry and diffusion tensor imaging. Magnetic resonance in medicine: official journal of the Society of Magnetic Resonance in Medicine/Society of Magnetic Resonance in Medicine. 2009; 61(5):1066–1072.

139. Li TQ, Yao B, van Gelderen P, Merkle H, Dodd S, Talagala L, Koretsky AP, Duyn J. Characterization of T(2)(star) Heterogeneity in Human Brain White Matter. Magnet Reson Med. 2009; 62(6):1652–1657.

140. Liu C. Susceptibility tensor imaging. Magnetic resonance in medicine: official journal of the Society of Magnetic Resonance in Medicine/Society of Magnetic Resonance in Medicine. 2010; 63(6):1471–1477.

141. Lee J, Shmueli K, Fukunaga M, van Gelderen P, Merkle H, Silva AC, Duyn JH. Sensitivity of MRI resonance frequency to the orientation of brain tissue microstructure. Proceedings of the National Academy of Sciences of the United States of America. 2010; 107(11):5130–5135. [PubMed: 20202922]

142. Lonsdale K. Diamagnetic anisotropy of organic molecules. Proceedings of the Royal Society of London Series a-Mathematical and Physical Sciences. 1939; 171(A947):0541–0568.

143. Lounila J, Ala-Korpela M, Jokisaari J, Savolainen MJ, Kesaniemi YA. Effects of orientational order and particle size on the NMR line positions of lipoproteins. Phys Rev Lett. 1994; 72(25): 4049–4052. [PubMed: 10056366]

144. Sati P, van Gelderen P, Silva AC, Reich DS, Merkle H, de Zwart JA, Duyn JH. Micro-compartment specific T2() relaxation in the brain. NeuroImage. 2013; 77:268–278. [PubMed: 23528924]

145. Wharton S, Bowtell R. Effects of white matter microstructure on phase and susceptibility maps. Magnetic resonance in medicine: official journal of the Society of Magnetic Resonance in Medicine/Society of Magnetic Resonance in Medicine. 2015; 73(3):1258–1269.

146. Li X, Vikram DS, Lim IA, Jones CK, Farrell JA, van Zijl PC. Mapping magnetic susceptibility anisotropies of white matter in vivo in the human brain at 7 T. NeuroImage. 2012; 62(1):314–330. [PubMed: 22561358]

147. Li W, Wu B, Avram AV, Liu C. Magnetic susceptibility anisotropy of human brain in vivo and its molecular underpinnings. NeuroImage. 2012; 59(3):2088–2097. [PubMed: 22036681]

148. Luo J, He X, Yablonskiy DA. Magnetic susceptibility induced white matter MR signal frequency shifts-experimental comparison between Lorentzian sphere and generalized Lorentzian approaches. Magnetic resonance in medicine: official journal of the Society of Magnetic Resonance in Medicine/Society of Magnetic Resonance in Medicine. 2013

149. van Gelderen P, Mandelkow H, de Zwart JA, Duyn JH. The anisotropy of myelin magnetic susceptibility. Proc Ann Meeting ISMRM. 2013:708.

150. Liu C, Li W, Wu B, Jiang Y, Johnson GA. 3D fiber tractography with susceptibility tensor imaging. NeuroImage. 2012; 59(2):1290–1298. [PubMed: 21867759]

151. Boesch C, Slotboom J, Hoppeler H, Kreis R. In vivo determination of intra-myocellular lipids in human muscle by means of localized 1H-MR-spectroscopy. Magnetic resonance in medicine: official journal of the Society of Magnetic Resonance in Medicine/Society of Magnetic Resonance in Medicine. 1997; 37(4):484–493.

152. Hwang SN, Wehrli FW. The Calculation of the Susceptibility-Induced Magnetic-Field from 3d Nmr Images with Applications to Trabecular Bone. Journal of Magnetic Resonance Series B. 1995; 109(2):126–145.

153. Sukstanskii AL, Yablonskiy DA. On the role of neuronal magnetic susceptibility and structure symmetry on gradient echo MR signal formation. Magnetic resonance in medicine: official journal of the Society of Magnetic Resonance in Medicine/Society of Magnetic Resonance in Medicine. 2014; 71(1):345–353.

154. van Gelderen P, de Zwart JA, Lee J, Sati P, Reich DS, Duyn JH. Nonexponential T(2) decay in white matter. Magnetic resonance in medicine: official journal of the Society of Magnetic Resonance in Medicine/Society of Magnetic Resonance in Medicine. 2012; 67(1):110–117.

155. Dortch RD, Harkins KD, Juttukonda MR, Gore JC, Does MD. Characterizing inter-compartmental water exchange in myelinated tissue using relaxation exchange spectroscopy. Magnetic resonance in medicine: official journal of the Society of Magnetic Resonance in Medicine/Society of Magnetic Resonance in Medicine. 2012

156. Du YP, Chu R, Hwang D, Brown MS, Kleinschmidt-DeMasters BK, Singel D, Simon JH. Fast multislice mapping of the myelin water fraction using multicompartment analysis of T2* decay at 3T: a preliminary postmortem study. Magnetic resonance in medicine: official journal of the Society of Magnetic Resonance in Medicine/Society of Magnetic Resonance in Medicine. 2007; 58(5):865–870.

157. Mezer A, Yeatman JD, Stikov N, Kay KN, Cho NJ, Dougherty RF, Perry ML, Parvizi J, Hua le H, Butts-Pauly K, Wandell BA. Quantifying the local tissue volume and composition in individual brains with magnetic resonance imaging. Nature medicine. 2013; 19(12):1667–1672.

158. Li X, van Gelderen P, Sati P, de Zwart JA, Reich DS, Duyn JH. Detection of demyelination in multiple sclerosis by analysis of relaxation at 7 T. NeuroImage: Clinical. 2015; 7:709–714. [PubMed: 26594617]

159. Wharton S, Bowtell R. Gradient echo based fiber orientation mapping using R2* and frequency difference measurements. NeuroImage. 2013; 83:1011–1023. [PubMed: 23906549]

160. Young IR, Khenia S, Thomas DG, Davis CH, Gadian DG, Cox IJ, Ross BD, Bydder GM. Clinical magnetic susceptibility mapping of the brain. Journal of Computer Assisted Tomography. 1987; 11(1):2–6. [PubMed: 3805423]

161. Edelman RR, Johnson K, Buxton R, Shoukimas G, Rosen BR, Davis KR, Brady TJ. MR of hemorrhage: a new approach. AJNR American journal of neuroradiology. 1986; 7(5):751–756. [PubMed: 3096097]

162. Sehgal V, Delproposto Z, Haacke EM, Tong KA, Wycliffe N, Kido DK, Xu Y, Neelavalli J, Haddar D, Reichenbach JR. Clinical applications of neuroimaging with susceptibility-weighted imaging. Journal of magnetic resonance imaging: JMRI. 2005; 22(4):439–450. [PubMed: 16163700]
163. Tong KA, Ashwal S, Obenaus A, Nickerson JP, Kido D, Haacke EM. Susceptibility-weighted MR imaging: a review of clinical applications in children. AJNR American journal of neuroradiology. 2008; 29(1):9–17. [PubMed: 17925363]
164. Mohammed W, Xunning H, Haibin S, Jingzhi M. Clinical applications of susceptibility-weighted imaging in detecting and grading intracranial gliomas: a review. Cancer imaging: the official publication of the International Cancer Imaging Society. 2013; 13:186–195. [PubMed: 23618919]
165. Lupo JM, Li Y, Hess CP, Nelson SJ. Advances in ultra-high field MRI for the clinical management of patients with brain tumors. Current opinion in neurology. 2011; 24(6):605–615. [PubMed: 22045220]
166. Sehgal V, Delproposto Z, Haddar D, Haacke EM, Sloan AE, Zamorano LJ, Barger G, Hu J, Xu Y, Prabhakaran KP, Elangovan IR, Neelavalli J, Reichenbach JR. Susceptibility-weighted imaging to visualize blood products and improve tumor contrast in the study of brain masses. Journal of magnetic resonance imaging: JMRI. 2006; 24(1):41–51. [PubMed: 16755540]
167. Bian W, Hess CP, Chang SM, Nelson SJ, Lupo JM. Susceptibility-weighted MR imaging of radiation therapy-induced cerebral microbleeds in patients with glioma: a comparison between 3T and 7T. Neuroradiology. 2014; 56(2):91–96. [PubMed: 24281386]
168. Sharp DJ, Ham TE. Investigating white matter injury after mild traumatic brain injury. Current opinion in neurology. 2011; 24(6):558–563. [PubMed: 21986682]
169. Versluis MJ, van der Grond J, van Buchem MA, van Zijl P, Webb AG. High-field imaging of neurodegenerative diseases. Neuroimaging clinics of North America. 2012; 22(2):159–171. ix. [PubMed: 22548926]
170. Liem MK, Lesnik Oberstein SA, Versluis MJ, Maat-Schieman ML, Haan J, Webb AG, Ferrari MD, van Buchem MA, van der Grond J. 7 T MRI reveals diffuse iron deposition in putamen and caudate nucleus in CADASIL. Journal of neurology, neurosurgery, and psychiatry. 2012; 83(12): 1180–1185.
171. Hingwala DR, Kesavadas C, Thomas B, Kapilamoorthy TR. Susceptibility weighted imaging in the evaluation of movement disorders. Clinical radiology. 2013; 68(6):e338–348. [PubMed: 23541097]
172. van Rooden S, Doan NT, Versluis MJ, Goos JD, Webb AG, Oleksik AM, van der Flier WM, Scheltens P, Barkhof F, Weverling-Rynsburger AW, Blauw GJ, Reiber JH, van Buchem MA, Milles J, van der Grond J. 7T T(2)*-weighted magnetic resonance imaging reveals cortical phase differences between early- and late-onset Alzheimer's disease. Neurobiology of aging. 2015; 36(1):20–26. [PubMed: 25113794]
173. Ignjatovic A, Stevic Z, Lavrnic S, Dakovic M, Bacic G. Brain iron MRI: a biomarker for amyotrophic lateral sclerosis. Journal of magnetic resonance imaging: JMRI. 2013; 38(6):1472–1479. [PubMed: 23564606]
174. Kwan JY, Jeong SY, Van Gelderen P, Deng HX, Quezado MM, Danielian LE, Butman JA, Chen L, Bayat E, Russell J, Siddique T, Duyn JH, Rouault TA, Floeter MK. Iron Accumulation in Deep Cortical Layers Accounts for MRI Signal Abnormalities in ALS: Correlating 7 Tesla MRI and Pathology. PloS one. 2012; 7(4):e35241. [PubMed: 22529995]
175. Bagnato F, Hametner S, Yao B, van Gelderen P, Merkle H, Cantor FK, Lassmann H, Duyn JH. Tracking iron in multiple sclerosis: a combined imaging and histopathological study at 7 Tesla. Brain: a journal of neurology. 2011; 134(Pt 12):3602–3615. [PubMed: 22171355]
176. Bian W, Harter K, Hammond-Rosenbluth KE, Lupo JM, Xu D, Kelley DA, Vigneron DB, Nelson SJ, Pelletier D. A serial in vivo 7T magnetic resonance phase imaging study of white matter lesions in multiple sclerosis. Multiple sclerosis. 2013; 19(1):69–75. [PubMed: 22641301]
177. Mainero C, Benner T, Radding A, van der Kouwe A, Jensen R, Rosen BR, Kinkel RP. In vivo imaging of cortical pathology in multiple sclerosis using ultra-high field MRI. Neurology. 2009; 73(12):941–948. [PubMed: 19641168]

178. Mainero C, Louapre C, Govindarajan ST, Gianni C, Nielsen AS, Cohen-Adad J, Sloane J, Kinkel RP. A gradient in cortical pathology in multiple sclerosis by in vivo quantitative 7 T imaging. Brain: a journal of neurology. 2015; 138(Pt 4):932–945. [PubMed: 25681411]

179. Pitt D, Boster A, Pei W, Wohleb E, Jasne A, Zachariah CR, Rammohan K, Knopp MV, Schmalbrock P. Imaging cortical lesions in multiple sclerosis with ultra-high-field magnetic resonance imaging. Archives of neurology. 2010; 67(7):812–818. [PubMed: 20625086]

180. Wiggermann V, Hernandez Torres E, Vavasour IM, Moore GR, Laule C, MacKay AL, Li DK, Traboulsee A, Rauscher A. Magnetic resonance frequency shifts during acute MS lesion formation. Neurology. 2013; 81(3):211–218. [PubMed: 23761621]

181. Yao B, Hametner S, van Gelderen P, Merkle H, Chen C, Lassmann H, Duyn JH, Bagnato F. 7 Tesla magnetic resonance imaging to detect cortical pathology in multiple sclerosis. PloS one. 2014; 9(10):e108863. [PubMed: 25303286]

182. Haacke EM, Makki M, Ge Y, Maheshwari M, Sehgal V, Hu J, Selvan M, Wu Z, Latif Z, Xuan Y, Khan O, Garbern J, Grossman RI. Characterizing iron deposition in multiple sclerosis lesions using susceptibility weighted imaging. Journal of magnetic resonance imaging: JMRI. 2009; 29(3):537–544. [PubMed: 19243035]

183. Yablonskiy DA, Luo J, Sukstanskii AL, Iyer A, Cross AH. Biophysical mechanisms of MRI signal frequency contrast in multiple sclerosis. Proceedings of the National Academy of Sciences of the United States of America. 2012; 109(35):14212–14217. [PubMed: 22891307]

184. Duyn JH. Frequency shifts in the myelin water compartment. Magnetic resonance in medicine: official journal of the Society of Magnetic Resonance in Medicine/Society of Magnetic Resonance in Medicine. 2014; 71(6):1953–1955.

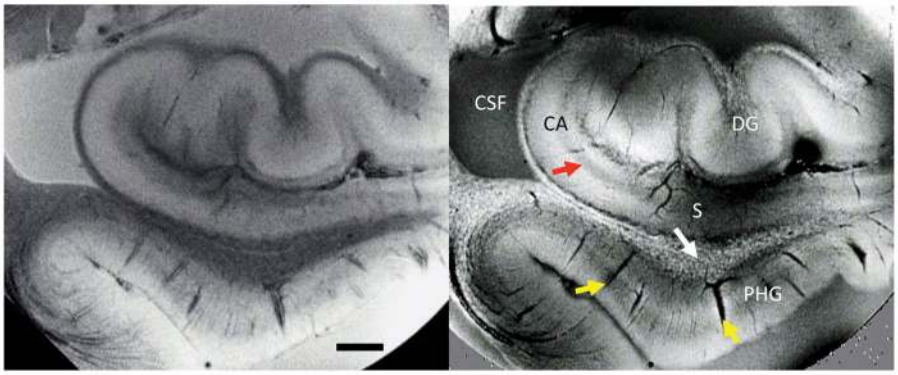

Figure 1.

SW MRI of ex-vivo hippocampal tissue. Signal amplitude (left) and phase (right) show distinctly different contrast. Regions such as dentate gyrus (DG), cornu ammonis (CA), subiculum (S), and parahippocampal gyrus (PHG) are readily identifiable. Strong contrast is seen in and around vessels (yellow arrows), at pyramidal cell layers (red arrow) and in white matter (speckles indicated with white arrow) attributed to iron in ferritin and deoxyhemoglobin. Measurements performed at 7 T, TE=30ms, 50x50x500mm resolution. Scale bar = 2 mm.

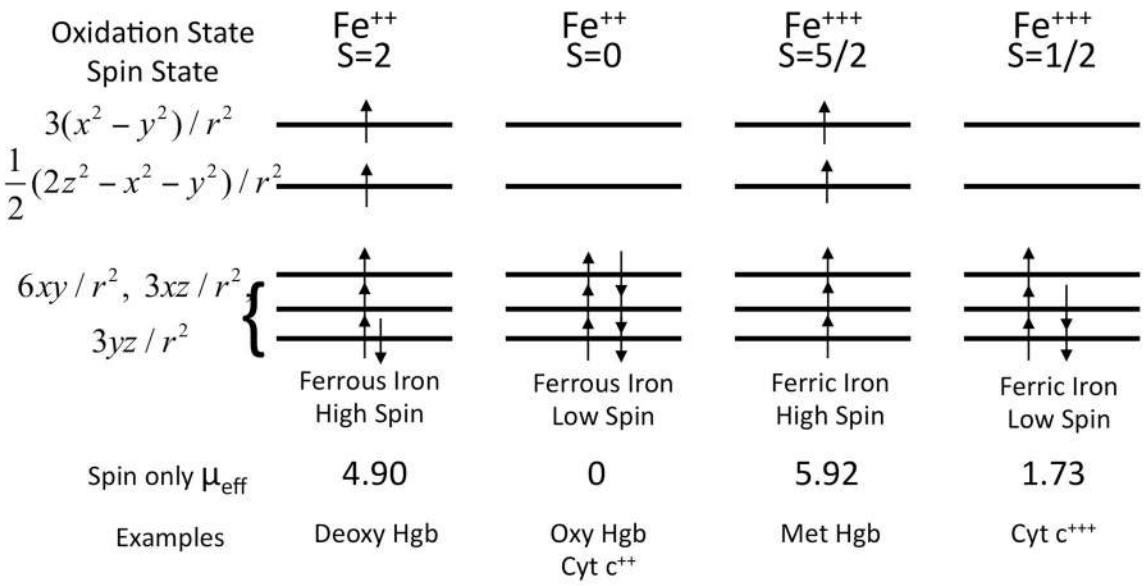

Figure 2.

Correlation of iron oxidation states with spin states. Using heme as an example, the diagram shows how the magnetic properties, determined by the total spin *S,* correlate with the oxidation states to produce high spin and low spin versions of both ferrous and ferric iron. Hgb refers to hemoglobin and cyt c^{++} refers to cytochrome c. Modified from: Perutz MF. Molecular anatomy, physiology, and pathology of hemoglobin. In: Stamatoyannopoulos G, editor. The molecular basis of blood diseases. Philadelphia: Saunders; 1987. p 127–178.

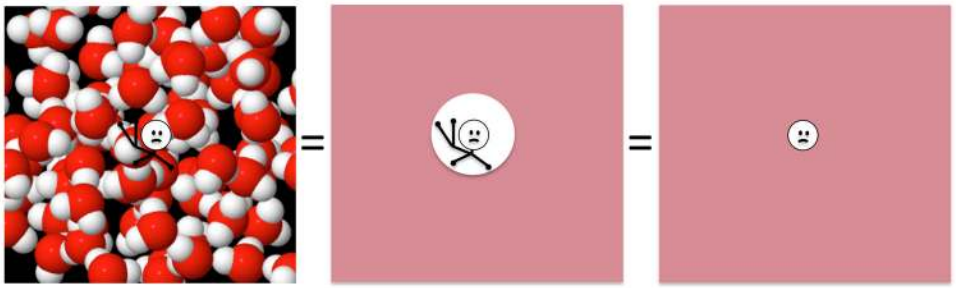

Figure 3.

Simplified model of magnetic environment of water proton (white sphere at center of each image) used to calculate the magnetic field it senses and the resulting MRI resonance frequency. Magnetic environment is assumed to result from nearby water dipoles, while effects from bonds (represented in chemical shift) are ignored. When considering the extensive averaging over the many sensing protons in a voxel, and the many rapidly moving magnetic sources of water molecules that surround them, the magnetic environment can be approximated by a continuum with a spherical cavity that for calculation purposes can be as small as the sensing proton. Molecular model of water courtesy of Michael Bruist, University of the Sciences, Philadelphia.

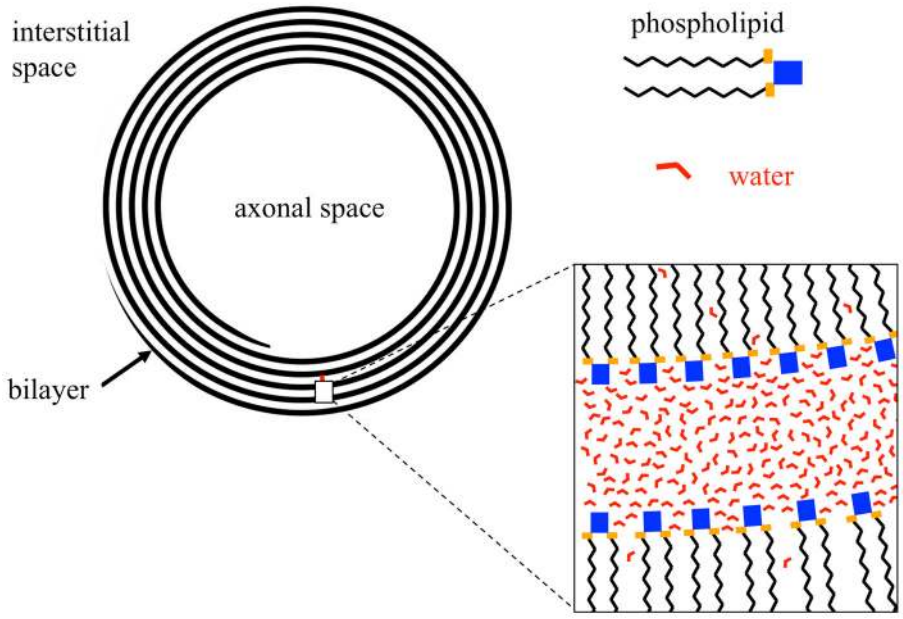

Figure 4.

Schematic cross section of axon showing location of myelin lipid bilayer and water. Within the myelin sheath, water is constrained to an approximately 4 nm wide space between successive bilayer wraps. Distinction between intra- and extracellular space of oligodendrocyte membrane is ignored in this schematic.

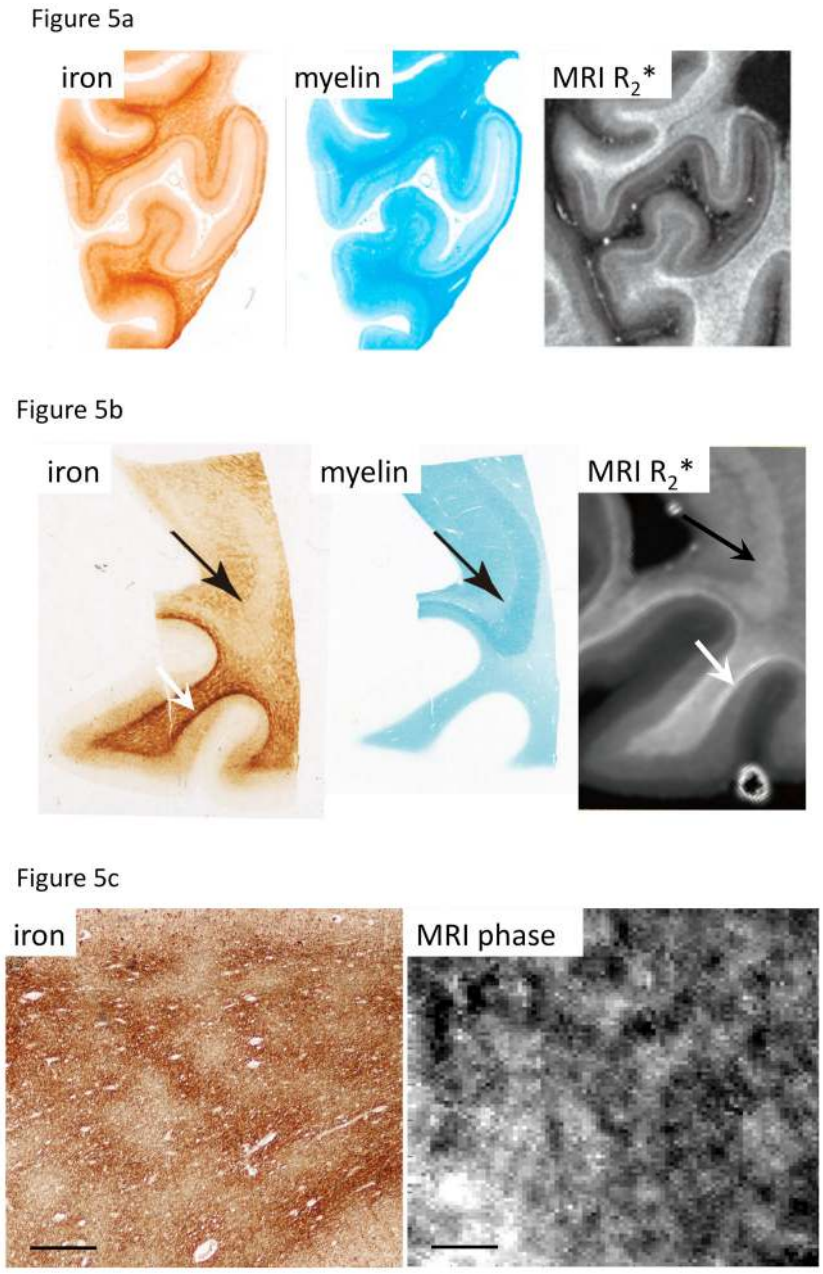

Figure 5.

Co-localization of iron and myelin, and appearance in SW MRI.

A. In cortical GM of the human occipital lobe, laminar variation in both iron and myelin is seen that is reflected in MRI R_2*. Substantial variation in iron is also seen in WM, with highest iron at the GM-WM boundary and otherwise a generally patchy distribution. These characteristics are also seen in MRI R_2*. Iron stain: Perls'/DAB; Myelin stain: luxol fast blue; MRI: 7 T, TE=15/30 ms, scale 0–100 s^{-1}. Reproduced from Fukunaga et al., PNAS 2010.

B. Varying contribution of iron and myelin to R_2*. Myelin appears to dominate MRI R_2* in the major WM fiber of the optic radiation (black arrows), whereas the reverse is true in the

WM immediately adjacent to the cortex (white arrow). Iron stain: Perls'/DAB; Myelin stain: luxol fast blue; MRI: 7 T, TE=15/30 ms, scale 0–80 s^{-1}. Reproduced from Fukunaga et al., ISMRM 2011, 12.

C. Investigation of patchy iron distribution in subcortical WM. Patchy iron distribution appears to be reflected in signal phase of SW MRI R_2* (from same tissue but slightly shifted area). Iron stain: Perls'/DAB; MRI: 11.7 T, TE=20 ms, 12.5 mm resolution. Scale bar = 100 mm. Reproduced from T-Q Li et al., ISMRM 2010, 2304.

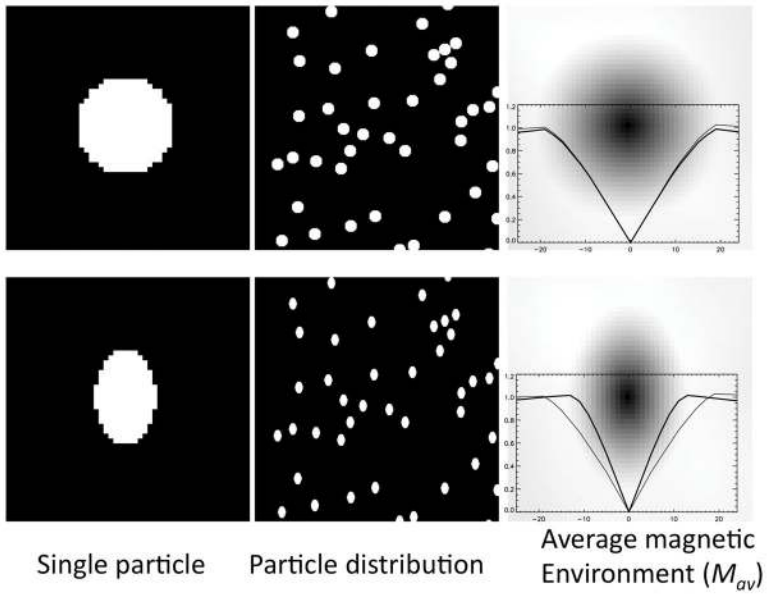

Figure 6.

Simulated (2D) average magnetic environment M_{aV} of a water proton in the presence of randomly distributed spherical (top row) or ellipsoidal (bottom row) magnetic particles. Single particles (left column) and M_{aV} (right column) are shown at 8-fold expanded scale. Brightness represents magnetization level; M_{aV} images include horizontal (thick line) and vertical (thin line) profiles through sensing nucleus at center. With the spherical particles, and with the uniformly oriented ellipsoidal particles, the average magnetic environment resembles the particle shape.. $M_{aV}(x,y)$ was calculated by adding the environments for all water pixel locations (i,j), and dividing the result by the number of water pixels N: $M_{aV}(x,y) = \Sigma_{i,j} M(x + i, y + j)/N$.

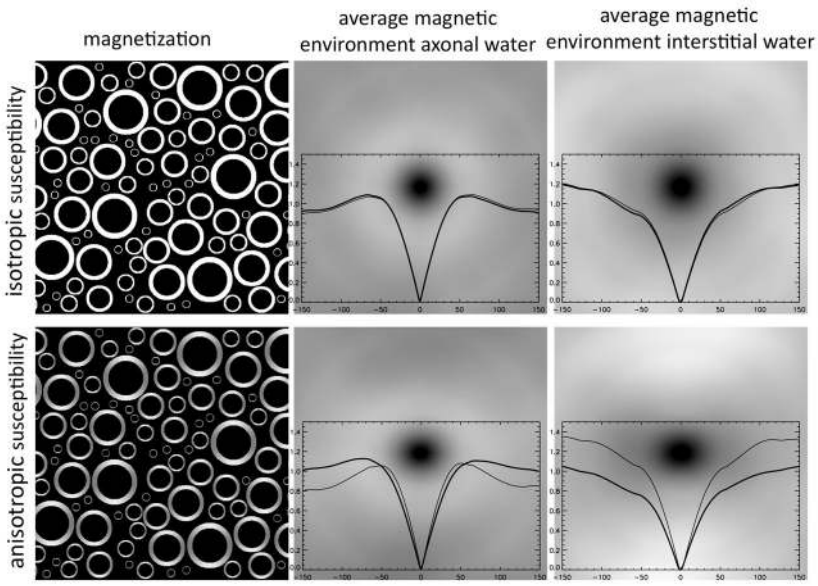

Figure 7.

Simulated (2D) average magnetic environment of a water proton inside and outside myelinated axons running perpendicular to the magnetic field (and the image plane). For isotropic susceptibility, both environments have cylindrical symmetry and lead to similar local fields (and thus frequencies). For anisotropic susceptibility, an asymmetry is observed that is reversed between the two water environments. This will lead to frequency differences between environments. Thick and thin plot lines show horizontal and vertical profiles respectively. Spatial scale of environment is 7-fold expanded compared to that of magnetization in left column. The average magnetic environment was calculated as described in caption of Fig. 6.

Table 1

Useful conversion factors (mM = millimol/liter = 6.02×10^{17} atoms/cc). A brain tissue density of 1g/cc is assumed.

1 μg Fe/g fresh tissue weight	1 ppm weight fraction Fe	1 μg Fe/cc	17.91 μM Fe
1 μg Cu/g fresh tissue weight	1 ppm weight fraction Cu	1 μg Cu/cc	15.74 μM Cu